Improving global mass flux solutions from Gravity Recovery and Climate Experiment (GRACE) through forward modeling and continuous time correlation

T. J. Sabaka, D. D. Rowlands, S.B. Luthcke, Jean-Paul Boy

Improving global mass flux solutions from Gravity Recovery and Climate Experiment (GRACE) through forward modeling and continuous time correlation

T. J. Sabaka,[1] D. D. Rowlands,[1] S. B. Luthcke,[1] and J.-P. Boy[1,2]

Received 8 March 2010; revised 26 May 2010; accepted 8 July 2010; published 10 November 2010.

[1] We describe Earth's mass flux from April 2003 through November 2008 by deriving a time series of mascons on a global 2° × 2° equal-area grid at 10 day intervals. We estimate the mass flux directly from K band range rate (KBRR) data provided by the Gravity Recovery and Climate Experiment (GRACE) mission. Using regularized least squares, we take into account the underlying process dynamics through continuous space and time-correlated constraints. In addition, we place the mascon approach in the context of other filtering techniques, showing its equivalence to anisotropic, nonsymmetric filtering, least squares collocation, and Kalman smoothing. We produce mascon time series from KBRR data that have and have not been corrected (forward modeled) for hydrological processes and find that the former produce superior results in oceanic areas by minimizing signal leakage from strong sources on land. By exploiting the structure of the spatiotemporal constraints, we are able to use a much more efficient (in storage and computation) inversion algorithm based upon the conjugate gradient method. This allows us to apply continuous rather than piecewise continuous time-correlated constraints, which we show via global maps and comparisons with ocean-bottom pressure gauges, to produce time series with reduced random variance and full systematic signal. Finally, we present a preferred global model, a hybrid whose oceanic portions are derived using forward modeling of hydrology but whose land portions are not, and thus represent a pure GRACE-derived signal.

Citation: Sabaka, T. J., D. D. Rowlands, S. B. Luthcke, and J.-P. Boy (2010), Improving global mass flux solutions from Gravity Recovery and Climate Experiment (GRACE) through forward modeling and continuous time correlation, *J. Geophys. Res.*, *115*, B11403, doi:10.1029/2010JB007533.

1. Introduction

[2] The Gravity Recovery and Climate Experiment (GRACE) mission [*Tapley et al.*, 2004] has vastly improved knowledge of the Earth's time-variable gravity field. Using data solely from the GRACE mission, it is possible to make unconstrained estimates of the Earth's gravity field represented as Stokes coefficients at 30 day intervals [*Tapley et al.*, 2004]. Although the Stokes coefficients described by *Tapley et al.* [2004] are estimated directly from GRACE tracking data without any constraints or a priori information, they are almost always smoothed or averaged (filtered) before use in geophysical analysis [see *Velicogna and Wahr*, 2006; *Wouters et al.*, 2008].

[3] Stokes coefficients from GRACE are estimated in a least squares solution by minimizing the difference between actual tracking observations and predictions that are computed based on the estimated coefficients. The effect of filtering is to increase the mismatch between actual observations and those predicted by the solution. Some filters do not take into account the covariance of the estimated Stokes coefficients and therefore cannot take into account any degradation in fit caused by the filtering (Gaussian smoothing is an example). *Klees et al.* [2008] argue that filtering of the GRACE Stokes coefficients is accomplished optimally by also taking into account the full covariance of the estimated Stokes coefficients. Certainly, when one has access to the full covariance of the solution as well as the estimated Stokes coefficients, it is possible to reconstruct the normal equations of the solution and thereby take into account the fit of the filtered solution.

[4] The widest possible variety of smoothing techniques is available given access to the original normal equations of the solution. Of course, it is not necessary to take the covariances into account, but access to the original normal equations opens up possibilities. For example, *Rowlands et al.* [2010] demonstrate that the normal equations of GRACE-based solutions can be augmented with constraint equations that yield outcomes that are as free of striping as those produced by Gaussian smoothing with much less loss of signal at high degrees.

[1] Planetary Geodynamics Laboratory, NASA Goddard Space Flight Center, Greenbelt, Maryland, USA.
[2] EOST-IPGS, UMR 7516 CNRS-UdS, Strasbourg, France.

0148-0227/10/2010JB007533

[5] It is interesting to note that global mascon solutions can be constructed starting from estimated Stokes coefficients and their covariances through a series of linear operators. In fact, the global mascon solutions that are presented in this paper are formed in just this way starting from the standard solutions (including the covariances) for Stokes coefficients that are routinely made at NASA's Goddard Space Flight Center (GSFC) [*Luthcke et al.*, 2006a]. As a result, these solutions belong to the class of solutions that are prepared by optimal filters as described by *Kusche* [2007] *Klees et al.* [2008]. It should also be noted that these global mascon solutions, like those shown by *Rowlands et al.* [2010], are filtered anisotropically through the use of regional constraint equations. In section 2 a mathematical development is given that places the approach that we use for our mascon solutions in the context of other filtering techniques commonly used by GRACE researchers such as anisotropic, nonsymmetric (ANS) filters, least squares collocation (LSC), and Kalman filtering/smoothing. A useful decomposition of the space/time constraint matrix is also given in section 2. This decomposition is exploited in section 3 where an efficient inversion scheme is developed. This allows us to estimate millions of time correlated parameters in a single inversion.

[6] In addition to placing our approach in the context of other GRACE filtering methods, a goal of this paper is to present status of global mascon solutions at GSFC, especially in light of two improvements to the procedure that produced the global mascon solutions presented by *Rowlands et al.* [2010]. The first improvement, the inclusion of the Global Land Data Assimilation System (GLDAS) hydrology model [*Rodell et al.*, 2004] in the a priori gravity model used in the GRACE tracking data reduction, is the subject of section 4. We demonstrate that the forward modeling of large hydrology signals over land areas has a significant effect on the ocean areas of the resulting solution. We present evidence that when signal from land hydrology is not included in the a priori gravity model, the resulting time series has spurious signal at the annual cycle over ocean areas. *Luthcke et al.* [2008] used forward modeling of hydrology in regional mascon solutions for Alaska. As far as we know, the time series presented in this paper are the first global, GRACE-based time series to use hydrology as a forward model in the Level 1B processing of KBRR data.

[7] In section 5 we discuss the second improvement, the use of continuous time correlation constraint equations for all of the parameters in a multiyear solution. Due to the computational burden involved with making time correlated solutions, our previous global mascon solutions use only piecewise time correlation. In the inversion scheme developed in section 3 the computational burden grows approximately linearly with the number of time periods in the time series in this study. The use of this inversion scheme allows us to extend the time correlation between months. We demonstrate that this results in a time series of mass flux that has an improved signal-to-noise ratio compared to our previous time series and agrees more closely with independent observations such as those given by ocean-bottom pressure sensors.

[8] Finally, in section 6 we present a strategy for producing a preferred global solution, a hybrid in which the oceans exhibit minimal leakage from land signal while the land is mostly determined by GRACE and is not obfuscated by forward modeling.

2. Mascons in the Context of Filtering Techniques for GRACE

[9] The mascon approach to model time-variable gravity is a time-space technique in which time is discretized into a series of nonoverlapping, finite intervals. Within these, gravity is represented by a linear combination of signals that would be generated by loading localized parcels of water (in centimeter equivalent water height) on the mean-Earth sphere [*Chao et al.*, 1987]. However, many groups doing mass flux research operate within the spectral domain by using the Stokes coefficients provided by the GRACE project [*Tapley et al.*, 2004]. Furthermore, these groups often apply smoothing filters ex post facto to time series of GRACE Stokes coefficients provided to them at some sampling rate [see *Velicogna and Wahr*, 2006; *Wouters et al.*, 2008]. Although *Rowlands et al.* [2010] present a geophysical comparison between Stokes coefficients derived from a typical post-processing technique versus the mascon technique, we wish here to place the comparison in a more mathematical framework in terms of operations on the Stokes coefficients, specifically in the context of the optimal ANS filters of *Kusche* [2007] and *Klees et al.* [2008]. Furthermore, temporal as well as spatial correlation between mascons have always been taken into account in GSFC regional mascon solutions and a large portion of this paper is devoted to showing how temporal correlation can be accomplished in global mascon solutions. Because of this we wish to place this technique in the context of linear dynamical systems theory and compare it with the Kalman filtering approach of *Kurtenbach et al.* [2009].

2.1. Anisotropic, Nonsymmetric Filters and Least Squares Collocation

[10] The GSFC mascon technique employs regularized least squares estimation to derive time series of equivalent water heights from GRACE KBRR residuals and can be transformed into filtering operations on time series of Stokes coefficients. Because it uses information about signal and noise covariance structure, it is an example of an "optimal" filter, and because the matrix which operates on Stokes coefficients is a function of both degree and order (anisotropic) and is nonsymmetric makes it an example of the most general form of these filters known as ANS [*Klees et al.*, 2008]. Thus, the ANS filter is a good point of comparison for all linear filters that operate on Stokes coefficients in space and time, even if they are not "optimal."

[11] *Klees et al.* [2008] define the input and output Stokes coefficient vectors, $\hat{\mathbf{c}}$ and $\tilde{\mathbf{c}}$, respectively, of the ANS filter, $\mathbf{F}$, in terms of the fundamental formula for LSC with noise [*Moritz*, 1980] given by

$$\tilde{\mathbf{c}} = \mathbf{F}\hat{\mathbf{c}} = \mathbf{P}^{-1}\left(\mathbf{N}^{-1} + \mathbf{P}^{-1}\right)^{-1}\hat{\mathbf{c}}, \tag{1}$$

where $\mathbf{P}^{-1}$ and $\mathbf{N}^{-1}$ are the signal and noise covariance matrices of the Stokes coefficients, respectively. Our task is then to cast the Stokes coefficients derived from the mascon approach into this form and we do this by introducing a matrix $\mathbf{L}$ that maps a set of mascon multipliers into a set of

Stokes coefficients describing the gravity perturbation through the well-known formula given by *Rowlands et al.* [2010].

[12] For a given 10 day period, we map 10,396 mascon multipliers, $\mathbf{m}$, into the 3720 Stokes coefficients, $\mathbf{c}$, of a degree/order (d/o) 60 spherical harmonic expansion (without monopole term) such that

$$\mathbf{c} = \mathbf{L}\mathbf{m}. \tag{2}$$

Here we are using the same mascon grid as in the work of *Rowlands et al.* [2010] where each parcel has a surface area equal to that of a 2° × 2° tesserae centered at the equator and every parcel spans a constant 2° latitude interval. This will be referred to simply as a "2° mascon grid" or a "q° mascon grid" in general. Now, assuming $\mathbf{L}$ is full rank, then let

$$\mathbf{L}^{\mathrm{T}} = \mathbf{Q}\mathbf{R} \tag{3}$$

be the QR decompositon of $\mathbf{L}^{\mathrm{T}}$ (the superscript "T" indicates the transpose), where $\mathbf{Q}$ has 3720 orthonormal columns and $\mathbf{R}$ is an upper-triangular matrix with nonzero diagonals [*Golub and Van Loan*, 1989]. We then define two related matrices

$$\mathbf{L}^{+} = \mathbf{Q}\left(\mathbf{R}^{\mathrm{T}}\right)^{-1} \tag{4}$$

and $\mathbf{L}_{\perp}$, where the 6676 columns of the latter are the orthonormal complement to the columns of $\mathbf{Q}$, which provide a complete basis in which any mascon solution may be expressed as

$$\mathbf{m} = \left(\mathbf{L}^{+}\ \mathbf{L}_{\perp}\right)\begin{pmatrix} \upsilon \\ \\ \zeta \end{pmatrix}. \tag{5}$$

Substituting equation (5) into equation (2) and using the properties of $\mathbf{L}$, $\mathbf{L}^{+}$, and $\mathbf{L}_{\perp}$ (that is, $\mathbf{L}\mathbf{L}^{+} = \mathbf{I}$ and $\mathbf{L}\mathbf{L}_{\perp} = 0$) shows that

$$\upsilon = \mathbf{c}, \tag{6}$$

and so we see that $\mathbf{L}^{+}$ provides a basis for mascons that corresponds directly with d/o 60 Stokes coefficients while $\mathbf{L}_{\perp}$ provides a basis for mascons that produce no gravity signature, i.e., a null-space that is not constrained directly by the GRACE KBRR data in our solution. We therefore relabel ζ as $\mathbf{c}_{\perp}$ and rewrite equation (5) as

$$\mathbf{m} = \left(\mathbf{L}^{+}\ \mathbf{L}_{\perp}\right)\begin{pmatrix} \mathbf{c} \\ \\ \mathbf{c}_{\perp} \end{pmatrix}. \tag{7}$$

[13] For a given 10 day period, let the GRACE KBRR residuals, $\mathbf{r}$, be defined as the difference between the KBRR measurements, $\mathbf{d}$, and a prediction, $\mathbf{a}(\mathbf{x}_c)$, which is a function of the current state of some general set of parameters, $\mathbf{x}_c$. These parameters can entail forward models, orbital arc parameters, geopotential parameters, etc. In section 4 we will explore the effects of changing the hydrology forward model in $\mathbf{x}_c$ on the mascon solution for this period, $\tilde{\mathbf{m}}$, taken as the unique minimizer of the quadratic cost function

$$J(\mathbf{m}) = (\mathbf{r} - \mathbf{A}\mathbf{L}\mathbf{m})^{\mathrm{T}}\widetilde{\mathbf{W}}(\mathbf{r} - \mathbf{A}\mathbf{L}\mathbf{m}) + \lambda\mathbf{m}^{\mathrm{T}}\mathbf{P}_{\mathbf{m}}\mathbf{m}, \tag{8}$$

where the first term is a measure of the weighted misfit to the KBRR residuals by the mascons and the second term is a measure of mascon complexity. Specifically, $\mathbf{A}$ is the Jacobian of the KBRR residuals with respect to the Stokes coefficients at the current state, $\widetilde{\mathbf{W}}$ is the data weight matrix which accounts for both measurement noise and the effects of orbital arc parameters (as will be shown later), $\mathbf{P}_{\mathbf{m}}$ is a regularization matrix, and λ is a damping parameter that controls the level of regularization on the mascon solution. The solution is then given by

$$\tilde{\mathbf{m}} = \left(\mathbf{L}^{\mathrm{T}}\mathbf{N}\mathbf{L} + \lambda\mathbf{P}_{\mathbf{m}}\right)^{-1}\mathbf{L}^{\mathrm{T}}\mathbf{A}^{\mathrm{T}}\widetilde{\mathbf{W}}\mathbf{r}, \tag{9}$$

where $\mathbf{N} = \mathbf{A}^{\mathrm{T}}\widetilde{\mathbf{W}}\mathbf{A}$. However, if $\mathbf{N}$ is invertible, then we can construct an unconstrained solution for Stokes coefficients during this period by minimizing $J(\mathbf{m})$ with equation (2) substituted into equation (8) and with $\lambda = 0$ such that

$$\hat{\mathbf{c}} = \mathbf{N}^{-1}\mathbf{A}^{\mathrm{T}}\widetilde{\mathbf{W}}\mathbf{r} \tag{10}$$

and substitute $\mathbf{A}^{\mathrm{T}}\widetilde{\mathbf{W}}\mathbf{r} = \mathbf{N}\hat{\mathbf{c}}$ into equation (9) to obtain

$$\tilde{\mathbf{m}} = \left(\mathbf{L}^{\mathrm{T}}\mathbf{N}\mathbf{L} + \lambda\mathbf{P}_{\mathbf{m}}\right)^{-1}\mathbf{L}^{\mathrm{T}}\mathbf{N}\hat{\mathbf{c}}. \tag{11}$$

Now, using equation (7) and the fact that

$$\begin{pmatrix} \mathbf{L} \\ \\ \mathbf{L}_{\perp}^{\mathrm{T}} \end{pmatrix} = \left(\mathbf{L}^{+}\ \mathbf{L}_{\perp}\right)^{-1}, \tag{12}$$

which follows from the properties prefacing equation (6) and the fact that $\mathbf{L}_{\perp}$ is an orthonormal basis orthogonal to $\mathbf{Q}$, we transform equation (11) as follows:

$$\begin{pmatrix} \tilde{\mathbf{c}} \\ \\ \tilde{\mathbf{c}}_{\perp} \end{pmatrix} = \begin{pmatrix} \mathbf{L} \\ \\ \mathbf{L}_{\perp}^{\mathrm{T}} \end{pmatrix}\left(\mathbf{L}^{\mathrm{T}}\mathbf{N}\mathbf{L} + \lambda\mathbf{P}_{\mathbf{m}}\right)^{-1}\mathbf{L}^{\mathrm{T}}\mathbf{N}\hat{\mathbf{c}}, \tag{13}$$

$$\begin{pmatrix} \tilde{\mathbf{c}} \\ \\ \tilde{\mathbf{c}}_{\perp} \end{pmatrix} = \begin{pmatrix} \mathbf{L} \\ \\ \mathbf{L}_{\perp}^{\mathrm{T}} \end{pmatrix}\mathbf{P}_{\mathbf{m}}^{-1}\mathbf{L}^{\mathrm{T}}\left(\lambda\mathbf{N}^{-1} + \mathbf{L}\mathbf{P}_{\mathbf{m}}^{-1}\mathbf{L}^{\mathrm{T}}\right)^{-1}\hat{\mathbf{c}}, \tag{14}$$

where we have assumed that $\mathbf{P}_{\mathbf{m}}$ is invertible. Through simple covariance propagation we see that

$$\mathbf{P}^{-1} = \mathbf{L}\mathbf{P}_{\mathbf{m}}^{-1}\mathbf{L}^{\mathrm{T}} \tag{15}$$

is the signal auto-covariance matrix for $\mathbf{c}$ and that

$$\mathbf{C}_{\perp} = \mathbf{L}_{\perp}^{\mathrm{T}}\mathbf{P}_{\mathbf{m}}^{-1}\mathbf{L}^{\mathrm{T}} \tag{16}$$

is the signal cross-covariance matrix between $\mathbf{c}_{\perp}$ and $\mathbf{c}$.

[14] The expression for $\tilde{\mathbf{c}}$ in equation (14) is now in the form of the ANS filter of equation (1) and represents a classic "filter" operation in the parlance of LSC while the associated expression for $\tilde{\mathbf{c}}_{\perp}$ represents a classic "filter/prediction" operation. Here "filtering" is a mapping between two members of the same space, i.e., d/o 60 Stokes coefficients, which optimally mitigates the effects of noise, while strict "prediction" is a mapping or extrapolation from one space to another that is based upon properties of the signals. The expression for $\tilde{\mathbf{c}}_{\perp}$ in equation (14) can always be

rewritten in terms of a strict "prediction" from a "filtered" $\tilde{\mathbf{c}}$ as [*Moritz*, 1980]

$$\tilde{\mathbf{c}}_{\perp} = \mathbf{C}_{\perp}\mathbf{P}\tilde{\mathbf{c}}, \tag{17}$$

and so the "filter/prediction" operation should now be apparent. Note that if $\tilde{\mathbf{c}}$ and $\tilde{\mathbf{c}}_{\perp}$ were not correlated, i.e., $\mathbf{C}_{\perp} = \mathbf{0}$, then nothing about the state of $\tilde{\mathbf{c}}_{\perp}$ could be "predicted" from the GRACE-derived $\tilde{\mathbf{c}}$ since this lies in a null-space that is not seen by GRACE in our model.

[15] The $\hat{\mathbf{c}}$ and $\mathbf{N}^{-1}$ of the GSFC ANS filter are derived directly from tracking data, the details of which are given by *Luthcke et al.* [2006a], and thus, $\mathbf{N}^{-1}$ is not only a full noise covariance matrix, but one that is consistent with the unconstrained Stokes coefficients $\hat{\mathbf{c}}$. The characteristics of the Stokes signal covariance matrix $\mathbf{P}^{-1}$ are manifested in the mascon regularization matrix $\mathbf{P_m}$ of equation (11), on which we now focus, but it will be seen to reflect a nonstationary, anisotropic signal process based upon geolocatable physical properties.

2.2. Regularization of the Mascon Solution

[16] An estimation of Stokes coefficients can be readily derived directly from the GRACE KBRR residuals as shown in equation (10). However, both the residuals and the model are prone to error. Although this is somewhat mitigated by the use of the data weight matrix $\widetilde{\mathbf{W}}$, it is only in a relative sense, and overfitting of some portions of $\mathbf{r}$ may be unavoidable. We address this by introducing regularization to the solution, i.e., the second term in $J(\mathbf{m})$ in equation (8), which has the effect of drawing the solution away from a state that overfits $\mathbf{r}$ toward a justified a priori state. *Rowlands et al.* [2010] essentially employ a Tikhonov first-order regularization [*Brooks et al.*, 1999] in time and space in solving for their mascon time series. The associated a priori state is thus a constant mascon state whose level is controlled by additional independent constraints. In this study, as in the study by *Rowlands et al.* [2010], this level is chosen to be zero.

2.2.1. Spatial Regularization

[17] For a given 10 day period, *Rowlands et al.* [2010] require that all distinct mascon differences be close to zero in a statistical sense through the use of weights which are assigned to each pair such that if both mascons reside in the same designated region, then the value is a function of distance between their centers. However, if the two mascons reside in different regions, then the weight is zero, and the constraint vanishes. This can be shown in matrix notation by introducing a constraint matrix, $\mathbf{D}$, whose form is a discrete first-difference operator in the space domain such that if the kth row of $\mathbf{D}$ constrains the ith and jth mascons, then

$$\mathrm{D}_{ki} = 1, \quad \mathrm{D}_{kj} = -1, \quad \mathrm{D}_{kq} = 0 \ \text{ for all } \ q \neq i,j. \tag{18}$$

For a set of N mascons, there are $N(N-1)/2$ pair-wise combinations or rows in $\mathbf{D}$. The constraint equations are then written as

$$\mathbf{0} = \mathbf{D}\mathbf{m} + \mathbf{e}, \tag{19}$$

where $\mathbf{e}$ is assumed to be a Gaussian distributed random error with mean $\mathbf{0}$ and covariance matrix $\mathbf{W}^{-1}$, which is denoted as $\mathbf{e} \sim \mathcal{N}(\mathbf{0}, \mathbf{W}^{-1})$.

[18] Specifically, let $\mathbf{W}$ be a diagonal matrix whose kth diagonal is chosen from a Laplacian distribution with center at zero and scale parameter D such that

$$\mathrm{W}_{kk} = \begin{cases} \exp\left(1 - \dfrac{d_{ij}}{D}\right) & , \mathcal{R}_i = \mathcal{R}_j \\ 0 & , \mathcal{R}_i \neq \mathcal{R}_j \end{cases}, \tag{20}$$

where d_{ij} is the distance between mascon centers and $\mathcal{R}_i$ and $\mathcal{R}_j$ are the region designations for the ith and jth mascons, respectively. These regions are chosen to reflect the varying properties of mass flux within and between geographic boundaries. This type of regional signal covariance was applied to mascon analysis in the study of mass flux in Alaskan glaciers by *Luthcke et al.* [2008] and was also used in the recent study of *Wu et al.* [2009].

[19] It turns out that even with these constraints, the indicated inversion in equation (11) does not exist. This is because the constant vector $\mathbf{1}$ is in the null-spaces of both $\mathbf{L}$ and $\mathbf{D}$. This means that a uniform layer of water of constant height over the sphere will not produce any observable gravity signal in the GRACE KBRR measurements; that is, this mascon distribution resides in the span of the columns of $\mathbf{L}_{\perp}$. It should be clear that the quantity $\mathbf{Dm}$ will remain unchanged if a constant vector is added to $\mathbf{m}$. We therefore add an additional constraint minimizing signal magnitude in the direction of $\mathbf{1}$ with a weight of w_1, which allows us to write the total set of constraint equations as

$$\begin{pmatrix} \mathbf{0} \\ 0 \end{pmatrix} = \begin{pmatrix} \mathbf{D} \\ \mathbf{1}^{\mathrm{T}} \end{pmatrix} \mathbf{m} + \begin{pmatrix} \mathbf{e} \\ e \end{pmatrix}, \tag{21}$$

where $e \sim \mathcal{N}(0, w_1^{-1})$. For brevity, we rewrite the augmented system of equation (21) as

$$\mathbf{0} = \overline{\mathbf{D}}\mathbf{m} + \overline{\mathbf{e}} \tag{22}$$

and introduce the diagonal matrix $\overline{\mathbf{W}}$ whose upper-left portion is $\mathbf{W}$ and whose lower-right diagonal is w_1. Given this, the associated mascon regularization matrix is given by

$$\mathbf{P_m} = \overline{\mathbf{D}}^{\mathrm{T}}\overline{\mathbf{W}}\overline{\mathbf{D}}. \tag{23}$$

The inverse of $\mathbf{P_m}$ exists and may be interpreted as a mascon signal covariance matrix in the context of LSC. As such, it represents a nonstationary, anisotropic signal process by virtue of the regional weighting just mentioned.

2.2.2. Spatiotemporal Regularization

[20] The discussion has so far been restricted to a single 10 day analysis period, but it can be easily extended to multiple periods. Therefore, all future references to equations (10) and (11) will assume the spatiotemporal versions, unless otherwise indicated. If the parameters are arranged in vectors such that mascon multipliers for a particular period are contiguous and the periods are in time order, then the data normal matrix $\mathbf{N}$ becomes block diagonal, with each block differing in correspondence to a different period, and $\mathbf{L}$, $\mathbf{L}^{+}$, and $\mathbf{L}_{\perp}$ become block diagonal, with each block identical for each period.

[21] The transition to multiple periods is more profound for the regularization matrix $\mathbf{P_m}$ for then it becomes a

function not only of space, but also of time. However, this additional temporal aspect is explained by simply broadening the definition of the constraint matrix **D** to now include constraint pairings across different times rather than just space. The total number of constraints can be computed now where N is the set of all mascons across time and space. The corresponding weight between the ith and jth mascons is now a function of both distance between mascon centers and time difference between mascon periods and is taken from a joint Laplacian distribution in space and time. The modification to **W** is

$$\mathrm{W}_{kk} = \begin{cases} \exp\left(2 - \frac{d_{ij}}{D} - \frac{t_{ij}}{T}\right) & , \mathcal{R}_i = \mathcal{R}_j \\ 0 & , \mathcal{R}_i \neq \mathcal{R}_j \end{cases}, \tag{24}$$

where t_{ij} is the positive time difference between mascons and T is a scale parameter. Note that time correlation is accounted for only within regions and that one could impose an additional rule analogous to the regional definitions, but in time. It should also be noted that the parameters D and T are referred to as the "correlation length" and "correlation time" by, for instance, *Rowlands et al.* [2010], but for the interested reader it will be seen in Appendix B that it may be more appropriate to call these the "characteristic length" and "characteristic time" of the a priori variance of pairwise mascon differences in space and time, respectively.

[22] The spatiotemporal first-difference operator admits a formal null-space that represents a uniform water layer over the sphere which is constant through time. We, however, simply replicate the constraint on the constant vector direction **1** at each time period, which means that time-varying series of uniform water layers over the sphere are dampened. Clearly, the formal null-space is in the range of these constraints, but they also add additional regularization to the solution. The result is an invertible $\mathbf{P_m}$ having an interesting structure based upon Kronecker products. This structure is central to two topics explored in this paper, (1) the relationship of our solution strategy to that of dynamical systems, discussed in section 2.3, and (2) the design of an efficient inversion scheme, discussed in section 3.

[23] The Kronecker product of two matrices, **A** and **B**, is defined to be [*Toutenburg*, 1982]

$$\mathbf{A} \otimes \mathbf{B} = \begin{pmatrix} a_{11}\mathbf{B} & \cdots & a_{1n}\mathbf{B} \\ \vdots & \ddots & \vdots \\ a_{m1}\mathbf{B} & \cdots & a_{mn}\mathbf{B} \end{pmatrix}, \tag{25}$$

where $\mathbf{A} = (a_{ij})$ is an $m \times n$ matrix. Properties of the Kronecker product may be found in the work of *Laub* [2005]. Using this definition, it can be shown that the mascon regularization matrix $\mathbf{P_m}$ is expressible as the sum of two terms $\mathbf{P_f}$ and $\mathbf{P_u}$. The first term is due to the spatiotemporal first-difference operator and is given by

$$\mathbf{P_f} = \mathrm{diag}(\mathbf{z}) \otimes \mathrm{diag}(\mathbf{s}) - \mathbf{Z} \otimes \mathbf{S}, \tag{26}$$

where the diag(·) operator makes a diagonal matrix with diagonal entries taken from a vector argument. If we denote the number of time intervals as K and the number of mascons within any given interval as N, then the $K \times K$ matrix **Z** and the $N \times N$ matrix **S** are defined in the context of **W** as

$$\mathrm{Z}_{ij} = \exp\left(1 - \frac{t_{ij}}{T}\right), \tag{27}$$

$$\mathrm{S}_{ij} = \begin{cases} \exp\left(1 - \frac{d_{ij}}{D}\right) & , \mathcal{R}_i = \mathcal{R}_j \\ 0 & , \mathcal{R}_i \neq \mathcal{R}_j \end{cases}, \tag{28}$$

and $\mathbf{z} = \mathbf{Z1}$ and $\mathbf{s} = \mathbf{S1}$ are vectors of row sums of the **Z** and **S** matrices, respectively. The second term is due to the damping of time-varying uniform water layers

$$\mathbf{P_u} = \mathbf{I} \otimes \mathbf{1}\mathbf{1}^{\mathrm{T}}. \tag{29}$$

Here **I** is the $K \times K$ identity matrix and **1** is a length N vector of ones.

2.3. Linear Dynamical Systems and Kalman Filtering

[24] Recall from equation (10) that one could assemble a set of Stokes coefficients independently at each of the K time intervals from only the GRACE KBRR data existing in that interval. However, an approach like this would neglect the time correlation between the coefficients in each interval imparted by the temporal dynamics of the mass flux processes in the system. In addition, these data are nonlinear functions of the underlying gravity state (that is, the Stokes coefficients), but we assume the linear-tangent approximation is sufficient and express rather the KBRR residuals as linear functions of differential adjustments to the Stokes coefficients, i.e., $\hat{\mathbf{c}}$. The solution for $\tilde{\mathbf{m}}$ in equation (11) is then an attempt to solve this linear dynamic inverse problem by a general least squares estimation of the entire spatiotemporal system in which the dynamics are accounted for through the $\mathbf{P_m}$ matrix.

[25] The classic Kalman filter/smoother can also be used to address this problem by considering the following pair of equations:

$$\begin{cases} \mathbf{m}_k = \mathbf{G}_{k-1}\mathbf{m}_{k-1} + \mathbf{u}_{k-1} \\ \mathbf{y}_k = \mathbf{H}_k\mathbf{m}_k + \mathbf{v}_k \end{cases}. \tag{30}$$

The first equation involves a prediction of the mascon state $\mathbf{m}_k$ at interval k from the state at the previous interval through a linear transition function $\mathbf{G}_{k-1}$ under the assumption that the dynamics of the system can be represented by a first-order Markov process with $\mathbf{u}_{k-1} \sim \mathcal{N}(\mathbf{0}, \mathbf{U}_{k-1})$. Here we have ignored the additional control term. The second equation relates measurements $\mathbf{y}_k$ in interval k to the mascon state through a linear model matrix $\mathbf{H}_k$ with $\mathbf{v}_k \sim \mathcal{N}(\mathbf{0}, \mathbf{V}_k)$. Both the filter and the smoother find the minimum mean square error estimate of $\mathbf{m}_k$, but the filter uses only past information through the kth interval in its estimate while the smoother uses information across all K intervals; though computationally twice as expensive, the smoother gives preferred estimates of $\mathbf{m}_k$.

[26] Recently, *Kurtenbach et al.* [2009] applied Kalman filtering to GRACE Level 1B data, with annual and semi-annual parts removed, in order to obtain a gravity field time series of Stokes coefficients at daily intervals over 2 years.

They assume stationary isotropic process noise in time and space and are guided by a hydrology model, with annual and semi-annual parts removed, in arriving at an exponential covariance function which is approximated by a first-order Markov process. We will now show that the solution of equation (11) provides a time series of global mascon sets derived from Kalman smoothing under a variable-order Markov process assumption; that is, $\mathbf{m}_k$ is related to $\mathbf{m}_j$ through transition function $\mathbf{G}_{k-1,j}$, $j = 1, \ldots, k-1$ such that the first part of equation (30) is rewritten as

$$\mathbf{m}_k = \sum_{j=1}^{k-1} \mathbf{G}_{k-1,j}\mathbf{m}_j + \mathbf{u}_{k-1}. \tag{31}$$

This higher-order capability allows for more complicated dynamics to be considered. Although we also use exponential covariances, which are appropriate for first-order Markov processes, we can readily modify the $\mathbf{Z}$ matrix of equation (27) to reflect higher-order processes mentioned by *Gelb* [1974].

[27] An nth order Markov process is usually introduced into the Kalman framework by expanding the state-space up to n-fold at each interval and adding hard equality constraints, thus transforming the problem to a larger, equivalent first-order process [*Zhang et al.*, 2005]. However, the general smoother reflecting equation (31) can be expressed simply as the batch least squares solution to the following over-determined set of observation equations

$$\begin{pmatrix} \overline{\mathbf{y}} \\ \overline{\mathbf{a}} \end{pmatrix} = \begin{pmatrix} \overline{\mathbf{H}} \\ \overline{\mathbf{G}} \end{pmatrix}\mathbf{m} + \begin{pmatrix} \overline{\mathbf{v}} \\ \overline{\mathbf{u}} \end{pmatrix}, \tag{32}$$

where $\overline{\mathbf{v}} \sim \mathcal{N}(\mathbf{0}, \overline{\mathbf{V}})$ and $\overline{\mathbf{u}} \sim \mathcal{N}(\mathbf{0}, \overline{\mathbf{U}})$ are assumed uncorrelated, and

$$\begin{cases} \overline{\mathbf{y}} = \begin{pmatrix} \mathbf{y}_1 \\ \vdots \\ \mathbf{y}_K \end{pmatrix}, \quad \overline{\mathbf{H}} = \begin{pmatrix} \mathbf{H}_1 & \cdots & 0 \\ \vdots & \ddots & \vdots \\ 0 & \cdots & \mathbf{H}_K \end{pmatrix}, \\ \overline{\mathbf{a}} = \begin{pmatrix} -\mathbf{m}_0 \\ 0 \\ \vdots \\ 0 \end{pmatrix}, \quad \mathbf{m} = \begin{pmatrix} \mathbf{m}_1 \\ \vdots \\ \mathbf{m}_K \end{pmatrix}, \\ \overline{\mathbf{G}} = \begin{pmatrix} -\mathbf{I} & 0 & \cdots & 0 \\ \mathbf{G}_{11} & -\mathbf{I} & \cdots & 0 \\ \vdots & \vdots & \ddots & \vdots \\ \mathbf{G}_{K-1,1} & \mathbf{G}_{K-1,2} & \cdots & -\mathbf{I} \end{pmatrix}, \\ \overline{\mathbf{u}} = \begin{pmatrix} \mathbf{u}_0 \\ \mathbf{u}_1 \\ \vdots \\ \mathbf{u}_{K-1} \end{pmatrix}, \quad \overline{\mathbf{v}} = \begin{pmatrix} \mathbf{v}_1 \\ \vdots \\ \mathbf{v}_K \end{pmatrix}, \\ \overline{\mathbf{U}} = \begin{pmatrix} \mathbf{U}_0 & 0 & \cdots & 0 \\ 0 & \mathbf{U}_1 & \cdots & 0 \\ \vdots & \vdots & \ddots & \vdots \\ 0 & 0 & \cdots & \mathbf{U}_{K-1} \end{pmatrix}, \\ \overline{\mathbf{V}} = \begin{pmatrix} \mathbf{V}_1 & \cdots & 0 \\ \vdots & \ddots & \vdots \\ 0 & \cdots & \mathbf{V}_K \end{pmatrix}. \end{cases} \tag{33}$$

The $\mathbf{m}_0$ vector is an a priori seed state that initiates the dynamic process. The mascon studies presented here and by *Rowlands et al.* [2010] do not use a seed, and so this condition is assigned infinite variance, i.e., $\mathbf{U}_0^{-1} = \mathbf{0}$.

[28] We now make a simple identification between quantities in equations (10) and (11) with those in equations (32) and (33) in order to place our mascon technique in the context of general Kalman smoothing. First, let $\mathbf{B}$ be the lower-triangular Cholesky factor of a matrix $\widetilde{\mathbf{Z}}$ defined in terms of the $\mathbf{Z}$ matrix of equation (27) such that

$$\widetilde{\mathbf{Z}} = \mathrm{diag}(\mathbf{z}) - \mathbf{Z} = \mathbf{B}^{\mathrm{T}}\mathbf{B}. \tag{34}$$

Since $\widetilde{\mathbf{Z}}$ has a null-space of dimension one, then $\mathrm{B}_{11} = 0$ and $\mathrm{B}_{jj} > 0, j = 2, \ldots, K$, and since $\mathbf{1}$ spans this null-space, then the row-sums of $\mathbf{B}$ vanish. This is related to the *LU* version of the Cholesky decomposition for a semi-definite matrix discussed, for instance, by *Higham* [1990]. This leads to

$$\begin{cases} \mathbf{y}_k = \begin{pmatrix} \mathbf{r}_k \\ \mathbf{0} \\ 0 \end{pmatrix}, \quad \mathbf{H}_k = \begin{pmatrix} \mathbf{A}_k\mathbf{L} \\ \mathbf{D} \\ \mathbf{1}^{\mathrm{T}} \end{pmatrix}, \\ \mathbf{G}_{k-1,j} = -\left(\dfrac{\mathrm{B}_{kj}}{\mathrm{B}_{kk}}\right)\mathbf{I}, \quad \mathbf{U}_{k-1} = \left(\mathrm{B}_{kk}^2\mathbf{S}\right)^{-1}, \\ \mathbf{V}_k = \begin{pmatrix} \lambda\widetilde{\mathbf{W}}_k^{+} & \mathbf{0} & \mathbf{0} \\ \mathbf{0} & (\mathrm{z}_k\mathbf{W})^{-1} & \mathbf{0} \\ \mathbf{0}^{\mathrm{T}} & \mathbf{0}^{\mathrm{T}} & w_1^{-1} \end{pmatrix}. \end{cases} \tag{35}$$

The GRACE KBRR residuals for interval k and the Jacobian of these with respect to the Stokes coefficients are denoted by $\mathbf{r}_k$ and $\mathbf{A}_k$, respectively. The $\mathbf{L}$ matrix applies here to a single time interval, the $\mathbf{W}$ matrix is now the one defined in equation (20), and $w_1^{-1} = 1$ throughout this study.

[29] The $\widetilde{\mathbf{W}}_k^{+}$ matrix is the generalized inverse [*Toutenburg*, 1982] of the data weight matrix $\widetilde{\mathbf{W}}_k$ for interval k. As mentioned earlier, this accounts not only for measurement noise but also for the effects of the orbital arc parameters. Each GRACE KBRR measurement has a theoretical precision of 10^{-6} m/s [*Rowlands et al.*, 2010] and so the a priori measurement variance is taken as $\alpha = 10^{-12}$ (m/s)^2. If $\widetilde{\mathbf{A}}_k$ is the Jacobian of $\mathbf{r}_k$ with respect to the arc parameters, $\mathbf{b}_k$, in interval k, then the GRACE contribution to the kth block diagonal of the normal equations may be written as

$$\frac{1}{\alpha}\begin{pmatrix} \widetilde{\mathbf{A}}_k^{\mathrm{T}}\widetilde{\mathbf{A}}_k & \widetilde{\mathbf{A}}_k^{\mathrm{T}}\mathbf{A}_k \\ \mathbf{A}_k^{\mathrm{T}}\widetilde{\mathbf{A}}_k & \mathbf{A}_k^{\mathrm{T}}\mathbf{A}_k \end{pmatrix}\begin{pmatrix} \mathbf{b}_k \\ \mathbf{m}_k \end{pmatrix} = \frac{1}{\alpha}\begin{pmatrix} \widetilde{\mathbf{A}}_k^{\mathrm{T}}\mathbf{r}_k \\ \mathbf{A}_k^{\mathrm{T}}\mathbf{r}_k \end{pmatrix}. \tag{36}$$

We may eliminate $\mathbf{b}_k$ from the state-space by performing elementary row operations on this system leaving the equivalent partitioned portion corresponding to $\mathbf{m}_k$ given by

$$\mathbf{A}_k^{\mathrm{T}}\widetilde{\mathbf{W}}_k\mathbf{A}_k\mathbf{m}_k = \mathbf{A}_k^{\mathrm{T}}\widetilde{\mathbf{W}}_k\mathbf{r}_k, \tag{37}$$

where

$$\widetilde{\mathbf{W}}_k = \frac{1}{\alpha}\left[\mathbf{I} - \widetilde{\mathbf{A}}_k\left(\widetilde{\mathbf{A}}_k^{\mathrm{T}}\widetilde{\mathbf{A}}_k\right)^{-1}\widetilde{\mathbf{A}}_k^{\mathrm{T}}\right]. \tag{38}$$

Thus, the effects of $\mathbf{b}_k$ may be mapped into the data weight matrix. Note, however, that the matrix inside the brackets is

a projection matrix and is rank deficient. It gives zero weight to the directions spanned by the columns of $\widetilde{\mathbf{A}}_k$. This corresponds to infinite variances in the associated data covariance matrix and prompts the use of the generalized inversion operator "+" in the expression for $\mathbf{V}_k$ in equation (35).

[30] The choice of fundamental spatial and temporal resolutions (2° mascon grid at a 10 day interval) are made based on spatiotemporal coherency structure in the KBRR residuals and the choices for T and D result from the regional mascon investigations of *Luthcke et al.* [2008]. It was found that choosing T and D close to the separation time and distance between adjacent mascons in time and space, respectively, which is to say $T = 10$ days and $D = 200$ km, provides a good compromise between misfit and signal structure (annual and trend) for a range of λ. These results were extrapolated to the global case by *Rowlands et al.* [2010] and we also adopt this value for D throughout, but do use T values of 10 and 20 days. In the course of our study we compare solutions using only intramonthly time correlation, as in the work of *Rowlands et al.* [2010], where we use their value of $\lambda = 2 \times 10^{-4}$, with those using continuous time correlation, where $\lambda = 1 \times 10^{-4}$. The relative decrease in λ offsets the additional constraints applied in the continuous case. A discussion of the dynamical properties and implications of the temporal and spatial constraints used in GSFC mascons solutions is presented in Appendices A and B.

2.4. Summary

[31] The GSFC mascon approach exhibits several advantages for modeling global mass flux. First, the spatial localization of the mascons allows for plausible signal covariance matrices to be constructed based upon geolocatable physical properties, particularly through the use of independent regions [*Rowlands et al.*, 2010]. Any regional constraints applied in a spectral approach would require a covariance propagation, as in equation (15), from a localization like mascons regardless. Although the weighting used in this study is isotropic in space and time within a given region, this is certainly not required. Second, many research groups are provided with a time series of Stokes coefficients whose derivation is outside of their control. Furthermore, they do not typically have access to the noise covariance matrices corresponding to these series [*Kusche*, 2007; *Klees et al.*, 2008]. Since we derive our mascon, and subsequently our Stokes coefficient, time series directly from tracking data, we have not only a full noise covariance matrix, but one that is consistent with the coefficients. This is an important point since the use of a distorted noise covariance matrix will result in a suboptimal filter $\mathbf{F}$ [*Kusche*, 2007]. Note that these latter advantages apply not only to spectral approaches, but to other space-domain approaches in which a third party provides only a time series and no quantification of its error characteristics.

[32] However, *Kusche* [2007] also points out that the inverse of the data normal matrix $\mathbf{N}^{-1}$ is not necessarily the actual noise covariance matrix reflected in the data due to unknown GRACE background model (tides, atmospheric pressure) errors. It is precisely this point that has motivated us to further investigate the removal of more complete background models (what we call forward modeling) such as hydrology in section 4, which is the largest signal remaining in the data analyzed by *Rowlands et al.* [2010].

[33] Finally, the mascon technique, including regularization, may be classified in terms of a Kalman smoother applied to a variable-order Markov process. This provides a general framework in which to address the global mass flux problem, and we shall see in section 3 how this can be made computationally feasible.

3. Inversion Scheme

[34] It should be clear that whether we solve for a time series of mascons $\tilde{\mathbf{m}}$ in equation (11) or Stokes coefficients $\tilde{\mathbf{c}}$ in equation (14) we will need to invert matrices which are dense and whose size grows quadratically with the number of time intervals of interest. Even at a modest resolution level of one month, this will result in several tens of intervals and render direct inversions of these matrices impractical. We are therefore motivated to look for an alternative inversion method, and we will see that the special structure of the $\mathbf{P_m}$ matrix makes iterative methods very attractive for our needs.

[35] During the period between April 2003 and November 2008 we analyzed 197 intervals of 10 day duration having acceptable GRACE KBRR measurements using a 2° mascon grid, amounting to 2,048,012 mascon parameters. We also estimate a daily set of three parameters (other nuisance parameters such as accelerometer biases are estimated in earlier steps of the processing) over the 1660 days included in this study, giving 2,052,992 total parameters. These parameters, as described by *Rowlands et al.* [2002], are essentially calibrations used for orbital arc refinement and are handled in the inversion scheme by the usual partitioned solution approach in which their Schur-complement matrix [*Demmel*, 1997] is produced, the mascons adjustment solutions are made, then backsubstitution is applied for daily parameter adjustments. Because the footprint of the Schur complement does not extend beyond that of $\mathbf{L}^{\mathrm{T}}\mathbf{N}\mathbf{L}$, the daily parameters do not impact the design of the inversion scheme and will not be discussed further.

[36] While the inversion indicated in equation (11) involves a dense matrix of the stated dimensions, inspection of equations (26) and (29) shows that only the second term, $-\mathbf{Z} \otimes \mathbf{S}$, in $\mathbf{P_f}$ extends beyond the block-diagonal footprint of $\mathbf{L}^{\mathrm{T}}\mathbf{N}\mathbf{L}$. Although the inverse of this term, $-\mathbf{Z}^{-1} \otimes \mathbf{S}^{-1}$, and the inverse of the remaining block-diagonal term are easily computable, the inverse of their sum is not. This suggests the use of an iterative inversion method that invokes the matrix only through matrix-vector multiplies. In particular, this involves the multiplication of $\mathbf{Z} \otimes \mathbf{S}$ with various vector quantities $\mathbf{x}$ whose size and ordering correspond to the mascon solution vector $\mathbf{m}$. This is greatly facilitated by the following property of Kronecker products [*Lev-Ari*, 2005]

$$(\mathbf{Z} \otimes \mathbf{S})\mathbf{x} = (\mathbf{Z} \otimes \mathbf{S})\mathrm{vec}(\mathbf{X}) = \mathrm{vec}(\mathbf{S}\mathbf{X}\mathbf{Z}), \tag{39}$$

where the vec(·) operator vectorizes a matrix by columns and $\mathbf{X}$ is an $N \times K$ matrix such that X_{ij} is a quantity corresponding to the ith mascon parameter in the jth time interval (recall that K is the number of time intervals and N is the number of mascons within any given interval). The operation count for

the expression on the left is of order $\mathcal{O}(N^2K^2)$, while that on the right is $\mathcal{O}(NK(N+K))$. For $N \gg K$, the speedup is a factor of $\mathcal{O}(K)$; for our case this is about 197. As for storage, the explicit $\mathbf{Z} \otimes \mathbf{S}$ requires $\mathcal{O}(N^2\,K^2)$ words while individually, $\mathbf{Z}$ and $\mathbf{S}$ together require $\mathcal{O}(N^2 + K^2)$ words. For $N \gg K$, the savings is a factor of $\mathcal{O}(K^2)$; for our case this is about 39,000.

[37] We have chosen the Preconditioned Conjugate Gradient (PCG) method for our iterative scheme because of its simplicity, minimal storage requirements, and good convergence properties, details of which are given by *Demmel* [1997] and *Golub and Van Loan* [1989]. The preconditioned version is chosen since the convergence rate is higher for system matrices with lower condition numbers or fewer extreme eigenvalues [*Demmel*, 1997]. Because information is so concentrated in the $N \times N$ block-diagonal portions of our system matrix in equation (11), it is natural to employ this as a preconditioner, which is known as block-Jacobi preconditioning. This effectively means that in addition to matrix-vector multiplications, we must also explicitly invert this preconditioner matrix at each iteration, but this can be expedited by initially computing and storing the associated Cholesky factors of each block.

[38] Given that $N \gg K$, this results in an inversion scheme whose storage requirements and operation count per iteration grow linearly to first order with the number of time intervals. This is much more favorable than the storage requirements and operation count of the Cholesky decomposition used by *Rowlands et al.* [2010] that grow quadratically and cubically, respectively, with the number of time intervals. In fact, it would require an iteration count of order $\mathcal{O}(NK^2)$ for the PCG method to match the operation count in the Cholesky method. We find, however, that to meet the termination criterion

$$\frac{\| \delta\mathbf{m}^j \|_2}{\| \mathbf{m}^j \|_2} \leq 0.1\%, \tag{40}$$

where $\|\cdot\|_2$ is the Euclidean norm and $\mathbf{m}^j$ and $\delta\mathbf{m}^j$ are the PCG solution and update vectors at the jth iteration, respectively, it typically requires about 20 iterations. A parallelized algorithm arrives at the solution in approximately 3 h of wall-clock time using 16 processors on the Linux cluster "Discover" of the NASA Center for Computational Sciences (NCCS) located at GSFC.

4. Forward Modeling of Hydrology

[39] There are various advantages to using models of time-variable gravity signal as part of the a priori force model (as a forward model) when processing GRACE Level 1B tracking data. Many GRACE-derived time series are based on monthly solutions, the ones in this paper are based on 10 day solutions, and *Kurtenbach et al.* [2009] have even produced a time series based on daily solutions. However, even daily solutions cannot capture short period (subdaily) variations in the gravity field caused by atmospheric effects. In order to prevent aliasing, it is necessary to employ forward models of any effect containing periods too short to be captured by the estimation period.

[40] The forward models of the global mascon solutions presented by *Rowlands et al.* [2010] were selected on the basis of the frequency content of the sources. The forward models of that previous study are used again in this study. Gravity variations from the atmosphere are modeled to d/o 90 at 3 h intervals derived from European Centre for Medium-Range Weather Forecasts (ECMWF) operational pressure grids. Ocean tides are modeled with the GOT4.7 tide model [*Ray*, 1999; *Ray and Ponte*, 2003]. The nonbarotropic response of the ocean to atmospheric pressure loading (derived from 6 hourly ECMWF atmospheric pressure and winds), is modeled to d/o 90 using MOG2D [*Carrere and Lyard*, 2003].

[41] Apart from frequency content of the signal, there can be other considerations for including sources of time-variable gravity in the forward model. Gravity estimation from satellite tracking data analysis is a nonlinear process, often requiring multiple iterations. It is always helpful to start the estimation process as close to the "truth" as is possible. Also, although the differential nature of the GRACE KBRR observations makes them ideal for isolating local features of the Earth's gravity field, there are limitations. *Rowlands et al.* [2010] show that the effect of 20 cm of water standing over a 4° × 4° block at the equator is still seen in KBRR data 800 km past the edge of the block. This can result in spatial aliasing (otherwise known as leakage) in estimated gravity fields. GPS data do not isolate gravity signal as well as KBRR data, so, when GRACE gravity solutions include GPS data (as often the case, although not for the solutions described in this paper), the leakage problem can be even more severe. All of this argues for exploring the suitability of various sources of time variable gravity signal for forward modeling.

[42] The time-variable gravity signal generated by hydrology is one of the largest components of change detected by GRACE [*Chen et al.*, 2005] and in some large areas, such as the Amazon basin, the annual amplitude of the hydrological signal, as given by the GLDAS hydrology model, reaches over 16 cm of equivalent water. Even so, none of the GRACE Mission Releases (01–04) of Level 2 monthly gravity fields have used hydrology information as part of their forward modeling [*Flechtner*, 2007]. It was presumed that no currently available hydrology model had sufficient accuracy and resolution for use as a forward model. In this section we will show that there is ample evidence that using the GLDAS/Noah hydrology model [*Rodell et al.*, 2004] in the a priori gravity model during processing of GRACE Level 1B tracking data has a beneficial effect on the resulting time series of mass flux.

[43] Before demonstrating the effect of using the hydrology forward model, some aspects of its implementation should be discussed. The hydrology model provides information about additional or surplus mass in 0.25° × 0.25° cells over land areas at 3 h intervals. The sum of mass over these cells in any time interval need not be zero, although the Earth is obviously a closed system. The average period of a trajectory computed using a snapshot of mass flux cells is a function of the cells of mass that are overflown during the interval of the snapshot. In order to compute the average period correctly and have a global model suitable for orbit computations, we need to ensure that the sum of mass change over the entire Earth surface is zero. To this end we place the total surplus or deficit of mass change over land areas into the oceans. At each interval each ocean cell is assigned the same "hydrology" value as every other ocean

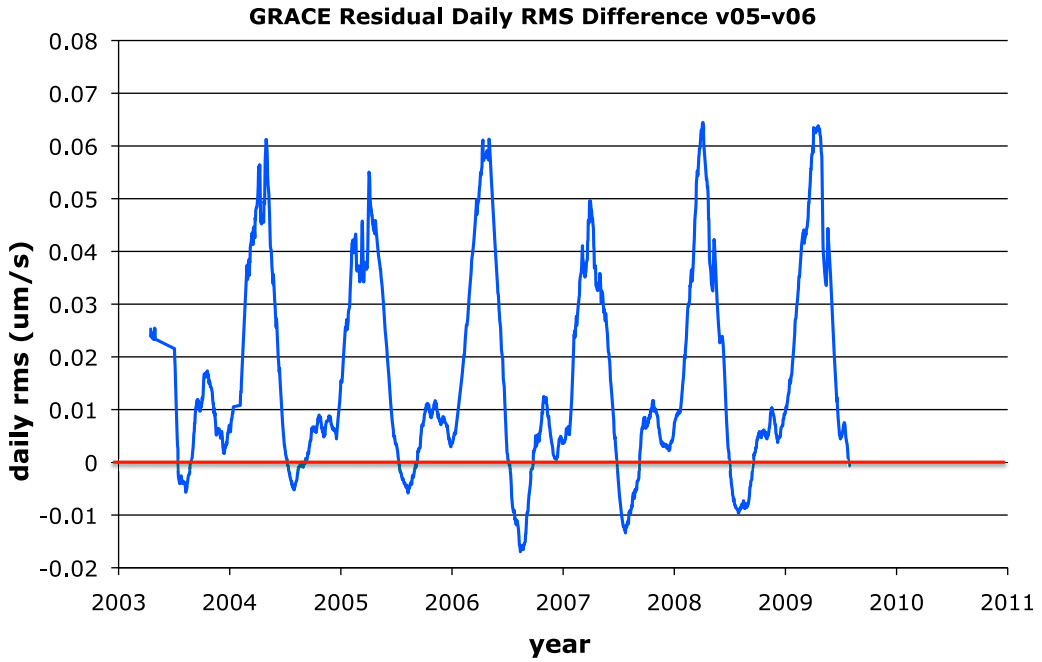

Figure 1. Difference in daily RMS of KBRR residuals used in the V05 (no hydrology forward modeled) and V06 (with hydrology forward modeled) normal equations, thus reflecting the effect of GLDAS hydrology. The blue line represents data that is smoothed using a 15 day moving average. A positive value indicates that the RMS of residuals of V05 is higher than that of V06.

cell and the sum over all of the ocean cells is equal in absolute value and opposite in sign to the sum over all of the land areas covered by the original hydrology model. In addition, as described by *Luthcke et al.* [2008], we have set the hydrology model to zero for the major mountain glacier areas and the Greenland and Antarctica ice sheets using a 0.25° mask. At each 3 h interval we create Stokes coefficients to d/o 90 from this global model of mass flux. These Stokes coefficients are then combined with other 3 hourly Stokes coefficients that correspond to atmosphere and ocean models. At every epoch of satellite force model computation the Earth's gravity field is represented by the sum of the Stokes coefficients from the mean gravity field and the 3 hourly gravity field.

[44] The first piece of evidence supporting the use of GLDAS hydrology as a forward model comes from the processing of Level 1B KBRR data during the creation of the normal equations for our gravity solutions. Residuals (the difference between actual observations and theoretical observations that are computed based on models) are a key component of any set of normal equations. The theoretical KBRR observations used for forming the residuals of our gravity normal-equations were computed using various models (including forward models of time-variable gravity) in daily solutions for parameters describing orbit initial state and accelerometer biases. The estimation of these parameters is based on minimizing the root mean square (RMS) of the KBRR residuals. The RMS of residuals from these solutions is a measure of many things, including the fidelity of forward models. For this investigation we have made multiple time series of mascons based on various solution strategies and for each time series we keep track of the RMS of the KBRR residuals used to form the normal equations. Among all of our time series of mascons we have two series that differ only in the forward modeling used during the daily generation of the KBRR residuals. One series, V06, uses the GLDAS hydrology model in the a priori gravity information and the other, V05, uses no hydrology model. Figure 1 shows the difference in the daily RMS of KBRR residuals used in the normal equations of these two time series. For the overwhelming majority of days the fit of the series using GLDAS hydrology is significantly better. For the relatively few time periods (always about midyear) where the GLDAS-based series has degraded fit, the degradation is minor. Apparently, the time-variable gravity signal contained in the GLDAS model is consistent with the KBRR observations.

[45] Figure 2 shows the standard deviation of the 197 estimated mascon values in each of 10396 cells in the 2° grid for the two time series. Looking at land areas (our global hydrology forward model has spatial variation only over land areas), it is clear that in general, the estimated mascon parameters of the GLDAS-based series are smaller in absolute value. In other words, the a priori values of the GLDAS-based mascon series are closer to the adjusted values over land (where mass signal used to generate a priori gravity was modeled) than their counterparts that did not use GLDAS as a forward model. There is no difference in the constraint information used in the solutions of the two time series, so the difference in the size of the adjustments in the two time series over land areas is a reflection of the distances between the a priori parameter values and the values detected by GRACE. In other words, the GLDAS hydrology model agrees fairly well with mass estimates derived from GRACE observations. This provides more evidence that the

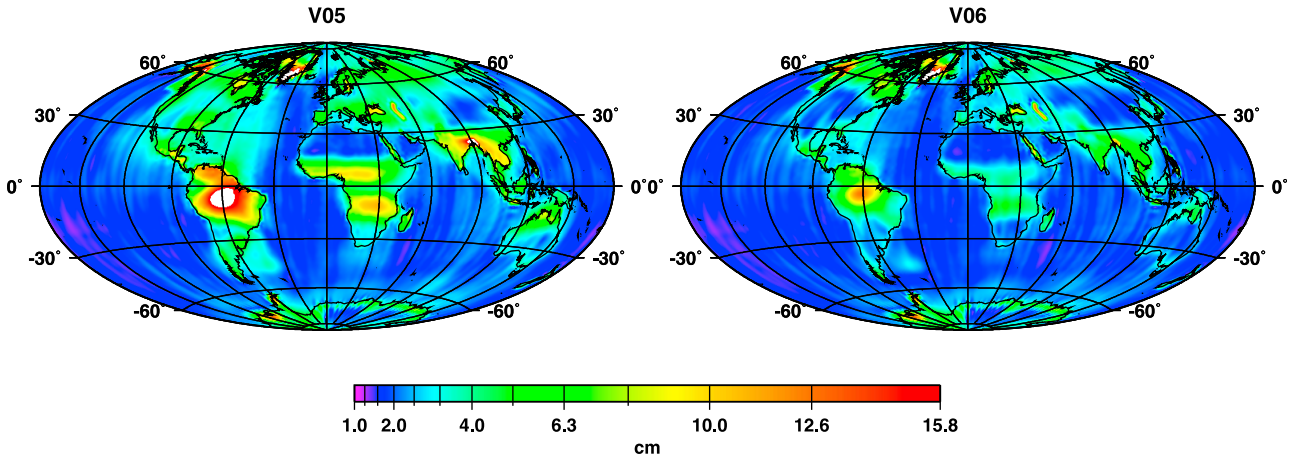

Figure 2. Standard deviation expressed in centimeters of equivalent water height for the V05 (no hydrology forward modeled) and V06 (with hydrology forward modeled) GRACE mascon solutions using T = 20 days and D = 200 km. White areas indicate values above the cutoff of 15.8 cm.

GLDAS hydrology can be used advantageously as a forward model.

[46] We note that although our global hydrology forward model has only temporal mass signal and no spatial signal over oceans, the two time series differ significantly (in magnitude and spatial distribution) over ocean areas (as can be seen by Figure 2). As is the case over land areas, over oceans the GLDAS-based mascons have smaller adjustments. In each ocean cell of the two time series we have estimated the annual signal (a phase and amplitude parameter at the annual frequency). Figure 3 shows the annual amplitude of each ocean cell of each of the two time series and the annual amplitude in the same cells for the GLORYS1V1 (GLobal Ocean ReanalYses and Simulations project) ocean model [*Drevillon et al.*, 2009]. The atmospheric and high-frequency oceanic forward models, that is, ECMWF and MOG2D, have been restored in the two GRACE solutions over the oceans in order to compare with the ocean circulation model [*Chambers*, 2006]. It is clear from these three plots that between the two mascon time series, the GLDAS-based time series (V06) has far less annual signal in the oceans. It is also clear that the annual amplitudes of the GLDAS-based mascon series agree much more closely with the ocean model. Furthermore, in the time series that did not use GLDAS hydrology (V05) several of the ocean areas with large annual amplitude are adjacent to land areas with large hydrological signal (for example, the Amazon basin).

[47] The use of GLDAS hydrology as a forward model has a significant effect on the time series of GRACE observed ocean surface mass. In Figure 4 we plot the time series of GRACE observed surface mass over the interior oceans, defined as 500 km from coast and between ± 66° latitude. The time series were computed using a calibrated spatial averaging kernel applied to the global mascon solutions represented as a time series of spherical harmonic coefficients to d/o 90 [*Swenson and Wahr*, 2002]. Virtually identical time series are obtained if a simple averaging of the interior ocean mascons is performed at each epoch. It is important to note that the time series do not represent ocean mass. They are the time series derived directly from the GRACE solutions and do not have the ocean model restored as well as the geocenter contribution. The annual signal in the time series that was estimated using a hydrology forward model, i.e., V06, has an amplitude that is 2 mm larger than that of V05. It is also a time series with less apparent noise. These differences in signal and noise are worth noting for researchers interested in ocean mass computations.

5. Continuous Time Correlation

[48] The GSFC regional mascon solutions have always exploited continuous time correlation, as can be seen in the work of *Rowlands et al.* [2005] and *Luthcke et al.* [2006b, 2008]. Recently, *Kurtenbach et al.* [2009] clearly quantified the improvements in global GRACE gravity solutions gained by exploiting continuous time correlation through Kalman filtering and in this paper we have demonstrated that our filter has a close relationship to this. The advantages of Kalman filtering likely apply to our implementation of continuous time correlation and vice versa, and in this section we present evidence similar to that of *Kurtenbach et al.* [2009] that this continuous scheme improves our solutions. We compare our newest global mascon solutions to those of *Rowlands et al.* [2010], where only correlations within individual months, i.e., intramonthly (IM), are considered, and show that extending time correlation across the entire time series, i.e., continuous (C), improves the signal-to-noise ratio over land areas (without loss of signal) and provides an improved solution over the oceans.

[49] We are comparing time series of mass flux from two solutions, both of which employ time correlation constraints. Our earlier solution (which is an extended time series of the yearlong time series presented by *Rowlands et al.* [2010]) uses time correlation constraints that are a proper subset of those used in our latest solution. Therefore, it is interesting to compare the signal and the noise in each solution. It is important to check whether the additional constraints of the second solution have decreased noise at the expense of decreasing signal.

[50] In order to compare the signal and noise characteristics of each solution, we examine the time series of mass change in each of the 10396 cells in the 2° grid. In the time

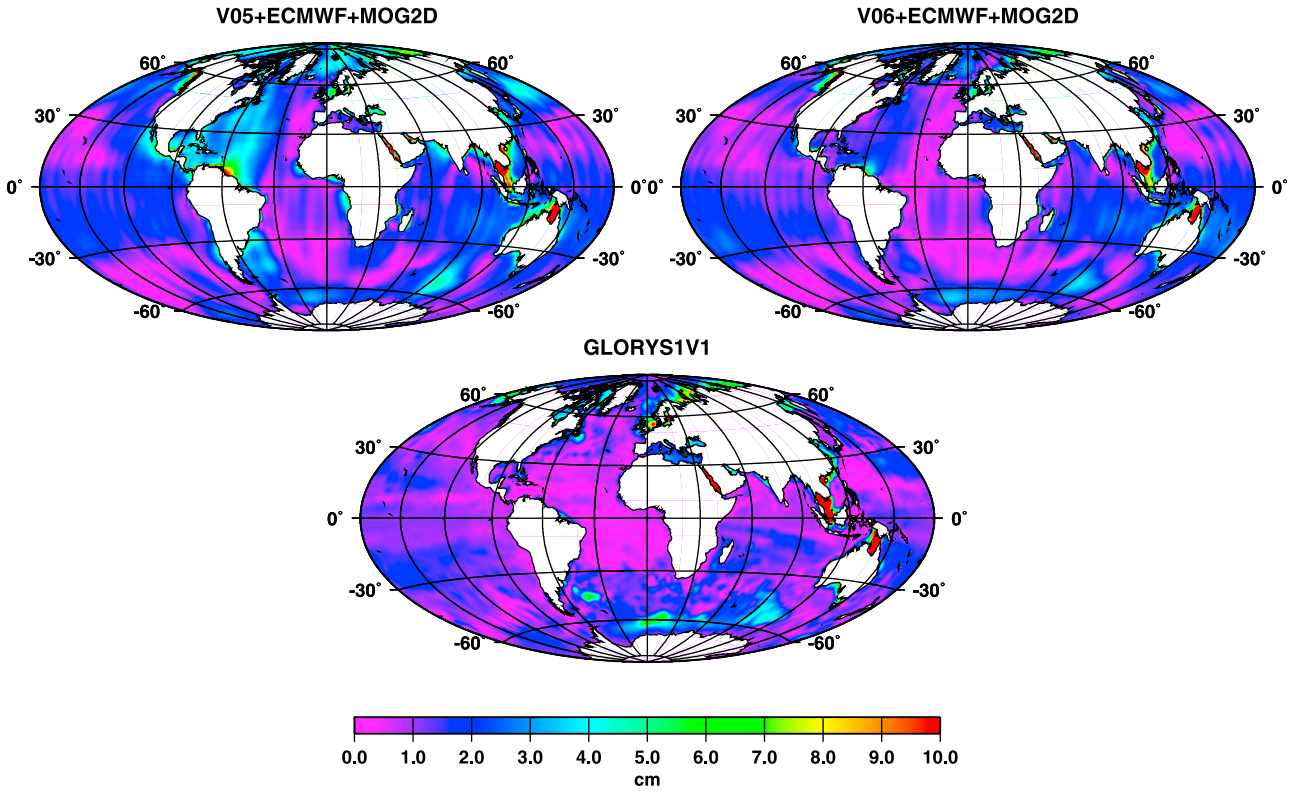

Figure 3. Annual amplitude over the oceans expressed in centimeters of equivalent water height for the V05 (no hydrology forward modeled) and V06 (with hydrology forward modeled) GRACE mascon solutions using $T = 20$ days and $D = 200$ km with the ECMWF and MOG2D signals restored and GLORYS1V1 modeled ocean-bottom pressure.

series of each solution there are 197 estimates of mass, one for each 10 day interval. For each of the 10396 separate time series we estimate four parameters: two linear parameters, and two parameters (a phase and amplitude) for the annual period. The rate and amplitude parameters are intended as a proxy for signal. As a proxy for noise in each cell we compute the RMS discrepancy between our four parameter function and the 197 mass estimates (we call this the "Fit"). Of course, the annual signal in each cell varies from year to year and we are estimating only an average annual signal, so the "Fit" is most likely an overestimate of the noise. For each cell we also compute the largest difference between adjacent 10 day period mass estimates (we call this the "Jump"). For each of the solutions we used the version of our processing that does not forward model hydrology (V05). In this way we can examine the largest signals. Table 1 gives the RMS statistics computed over various land cells for the two signal indicators and the two noise indicators. The four signal and noise indicators are given over three sets of land regions: all 2969 land cells, an area of 261 land cells close to the Amazon, and the 43 land cells corresponding to Greenland. The Greenland and Amazon regional subsets are chosen for display because they are known to have large signals.

[51] It is clearly demonstrated in Table 1 that the additional constraints employed for continuous time correlation do not result in loss of signal, but do reduce noise. Greenland is the area where the continuous time correlation appears to reduce noise the most. This is likely due to the relationship between time and space constraints. As mentioned in section 1 (more details are given by *Rowlands et al.* [2010]), each cell in our grid belongs to 1 of 25 regions within (but not between) which spatial constraints are used. The 261 Amazon cells of Table 1 belong to the greater South American region of our solution that has a total of 362 cells all tied together by spatial constraints. The 43 Greenland cells belong to two separate regions (interior highlands and coastal lowlands). Greenland is an area in which the characteristics of mass change vary quickly from cell to cell. To avoid losing this spatial variation, we cannot tie as many cells together as we do in the Amazon. The Greenland region of our solution is by nature noisier without the aid of additional temporal constraints. In other words, time correlation is more important in regions of high spatial variability.

[52] We present two more pieces of evidence that additional time constraints improve our solutions over ocean areas. The first piece of evidence is given by the standard deviation of the mass flux of the two solutions shown in Figure 5; one is a continuous time correlation case and the second uses intramonthly correlation only (as in the work of *Rowlands et al.* [2010]). The time series produced using only intramonthly correlation has many more longitudinal streaks, averaging about 4–5 cm, than the continuous case, and shows much more leakage in the Caribbean Sea area. These longitudinal streaks and leakage are almost certainly not signal.

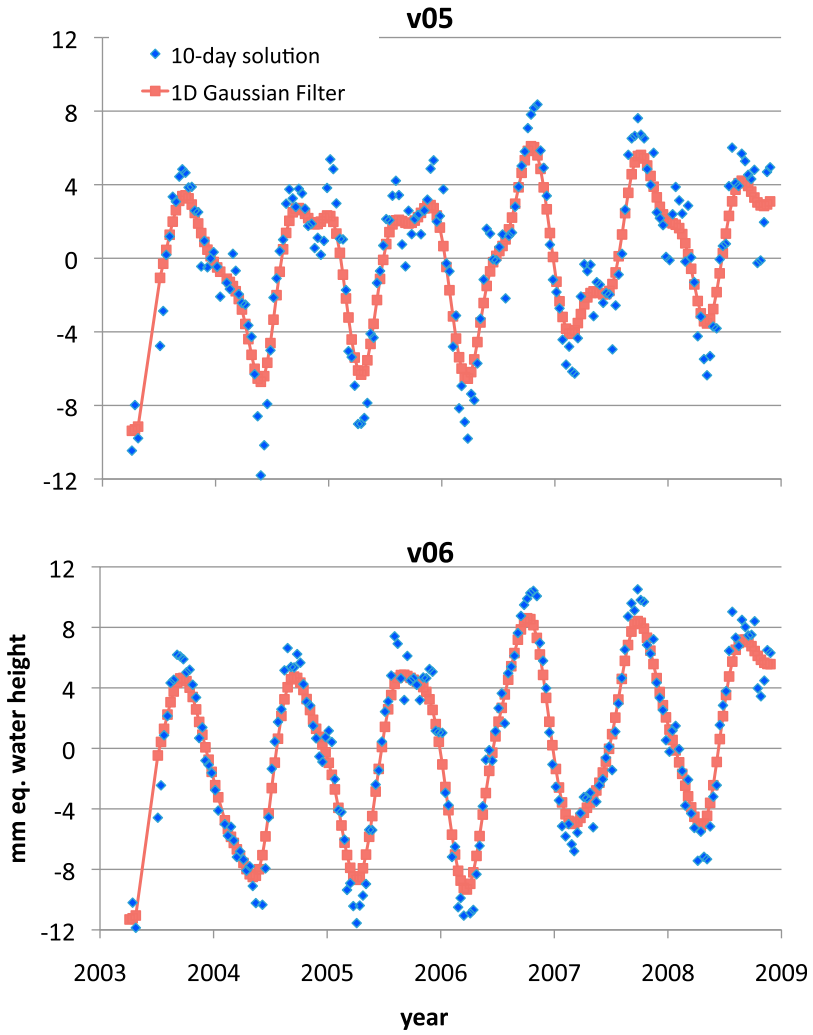

Figure 4. The time series of GRACE observed surface mass over the interior oceans, defined as 500 km from coast and between ± 66° latitude, for the V05 (no hydrology forward modeled) and V06 (with hydrology forward modeled) solutions. The blue dots represent the actual 10 day values, and the red curve represents a 1-D Gaussian smoothing of the 10 day values.

[53] As a final indication of the improvement gained through continuous time correlation, we compare two mascon derived time series having different time correlation constraints with ocean-bottom pressure (OBP) records at 14 locations that are depicted in Figure 6. In order to make a comparison with a mascon time series, the OBP records are prepared to correspond to mascon values. Tides are removed from the individual OBP records (tides are modeled in our Level 1 GRACE processing) and then averages are formed over 10 day periods corresponding to the mascon intervals. The tide-free 10 day average OBP values are then compared against a mascon value extracted from the 10 day period and 2° cell corresponding the OBP value. No smoothing or averaging of mascon values is done. However, as in the comparison with the ocean model, the ECMWF and MOG2D contributions are restored to the mascon values.

[54] For each of the three time series (two mascon and one OBP) we also formed the time series composed of first differences. The agreement (or lack of agreement) at long wavelength will be better represented by comparisons

Table 1. Signal and Noise Statistics Over Land for V05 (No Hydrology Forward Modeled) Continuous (C) and Intramonthly (IM) Time Correlation Solutions

		Trend (cm/yr)		Ann Amp (cm)		Jump (cm)		Fit (cm)	
Region	Number of Cells	C	IM	C	IM	C	IM	C	IM
All land	2969	1.87	1.86	7.92	7.82	12.39	14.61	4.16	4.58
Amazon	261	1.04	0.89	17.86	17.14	13.74	16.33	4.95	5.24
Greenland	43	9.85	9.70	5.95	5.93	16.98	34.47	6.87	8.96

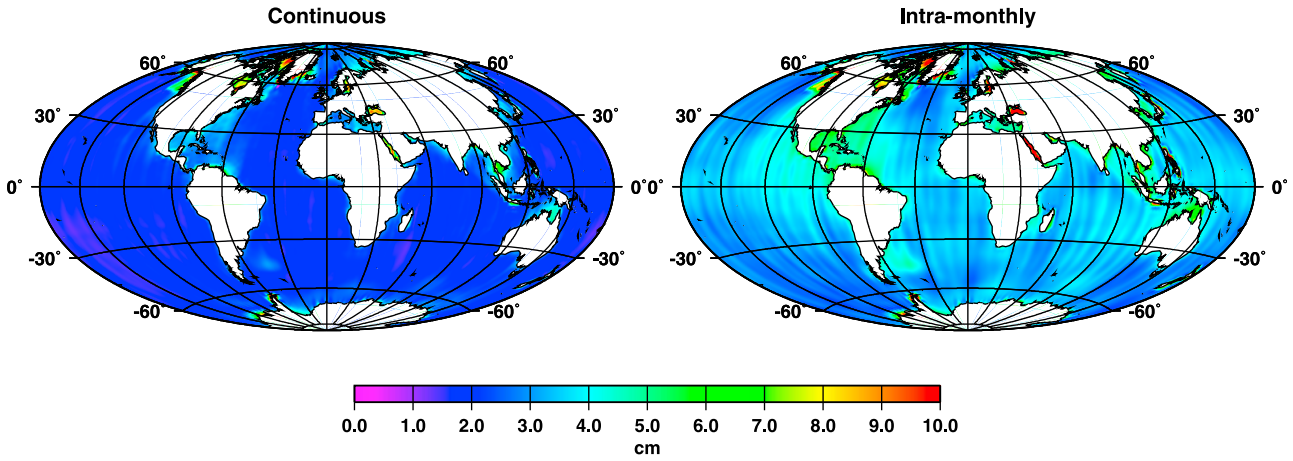

Figure 5. Standard deviation over the oceans expressed in centimeters of equivalent water height for the V06 (with hydrology forward modeled) (left) continuous and (right) intramonthly time-correlated GRACE mascon solutions using T = 20 days and D = 200 km.

between the original time series. The agreement at short wavelength will be better represented by comparisons of the first differences. Our mascon time series are posted every 10 days and so we are especially interested in the short wavelength agreement. Also, any possible drifts in the OBP sensors are less likely to affect the comparisons of first differences.

[55] Table 2 gives comparisons between OBP records (prepared as described above) and two solutions. The comparisons are in the form of correlations between each solution time series and the OBP time series as well as correlations between the first-differences. The two solutions compared against OBP records (V06-C and V06-IM) have hydrology forward modeled and differ only in the number of time correlation constraint equations used. The V06-C series uses continuous time correlation constraints and the V06-IM series, like the 2° mascon solution described in the work of *Rowlands et al.* [2010], has only intramonthly time correlation constraints. In general (at 12 out of the 14 sites), the V06-C time series has higher correlations than the V06-IM series that uses time constraints only within months. The comparison of the first differences of the series further vindicates the use of continuous time correlation. The first-difference correlations are generally higher than the undifferenced correlations (for both series) and the V06-C first-difference correlations are always higher than those of the V06-IM series. Figure 7 shows the OBP sensor time series along with the two GRACE time series with different time correlation strategies at six sites. The means of the time

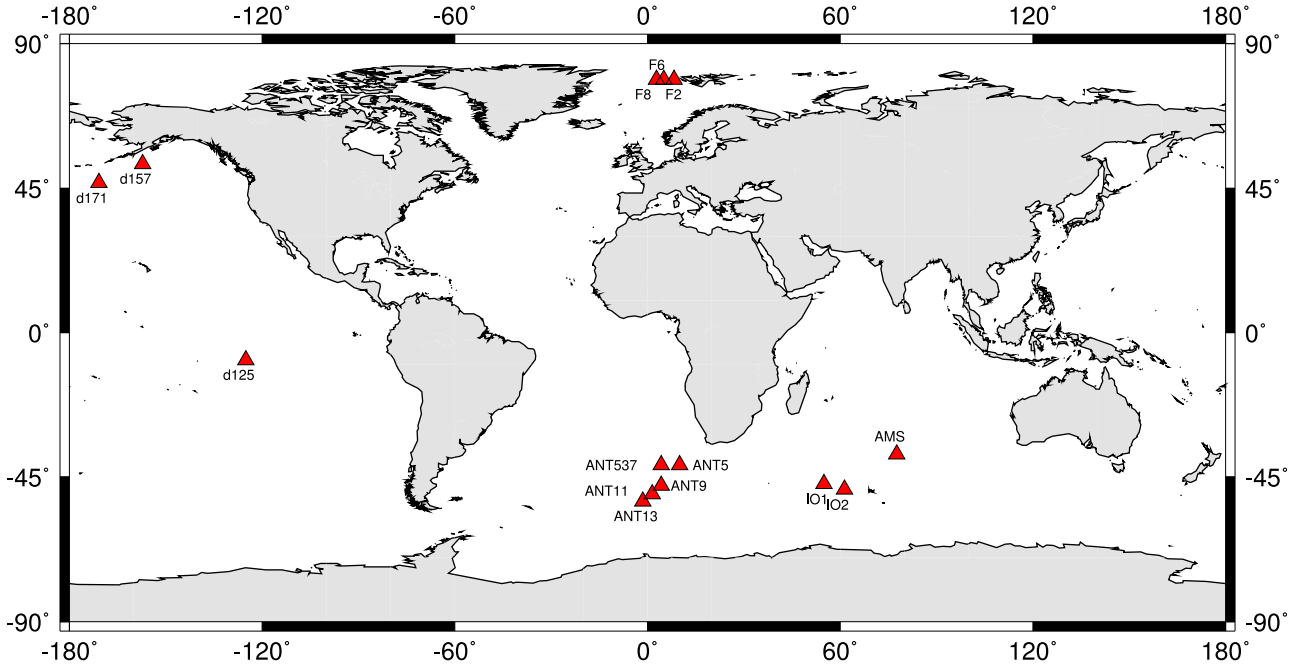

Figure 6. Locations of the 14 ocean-bottom pressure gauges examined in this study.

Table 2. Correlations Among Time Series and Among Their First Differences From 14 Ocean-Bottom Pressure Gauges and the V06 (With Hydrology Forward Modeled) Continuous (C) and Intramonthly (IM) Time Correlation Solutions

			Time Series		First Differences	
Gauge	Number of Samples	Span (years)	C	IM	C	IM
AMS	56	2003.26–2004.99	0.52	0.35	0.57	0.47
ANT11	78	2003.26–2007.32	0.52	0.53	0.45	0.41
ANT13	48	2006.82–2008.13	0.73	0.61	0.72	0.67
ANT5	110	2005.07–2008.10	0.32	0.25	0.29	0.24
ANT537	53	2006.65–2008.10	0.37	0.35	0.44	0.37
ANT9	110	2005.10–2008.13	0.32	0.17	0.61	0.55
F2	71	2004.68–2006.62	0.47	0.35	0.72	0.54
F6	101	2003.73–2006.62	0.56	0.48	0.77	0.65
F8	100	2003.73–2006.62	0.53	0.44	0.73	0.60
IO1	38	2004.10–2005.13	0.51	0.53	0.60	0.58
IO2	37	2004.10–2005.10	0.53	0.46	0.75	0.70
d125	34	2003.26–2004.37	0.18	0.00	−0.05	−0.20
d157	33	2003.26–2004.35	0.56	0.38	0.64	0.47
d171	33	2003.26–2004.35	0.52	0.38	0.42	0.27

series are artificially separated so that it easier to see how the features of each time series compare.

6. Global Solution Strategy

[56] We wish to present a solution that is determined mainly from GRACE observations. In this paper we establish that there are advantages to using GLDAS hydrology as a forward model, however, it does conflict somewhat with our goal of deriving a solution for mass flux primarily from the GRACE observations. Over land we use the GLDAS hydrology model at a very high spatial resolution (0.25°) and temporal resolution (3 h) and in many locations the

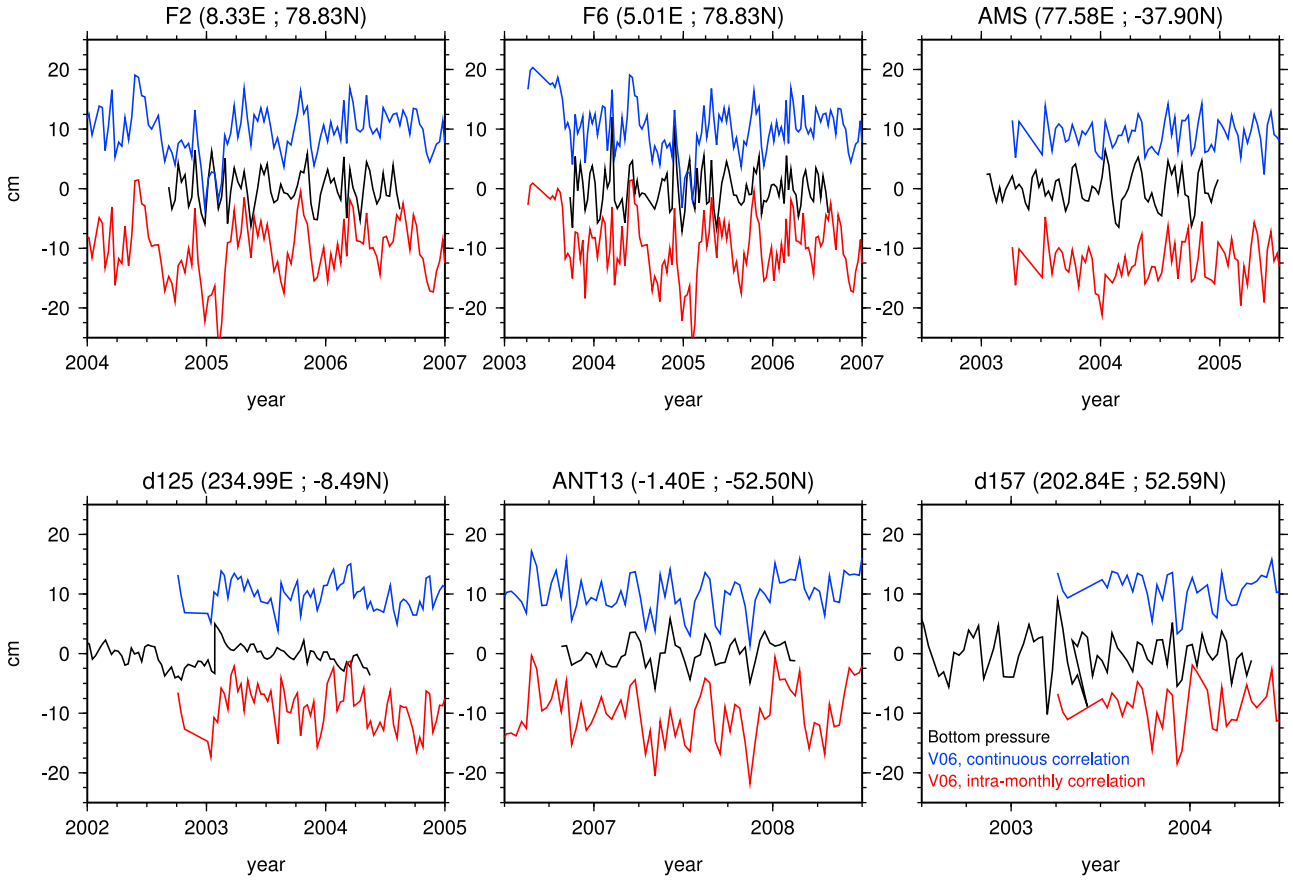

Figure 7. The 10 day averaged OBP time series of six selected gauges and the two corresponding V06 (with hydrology forward modeled) time series (continuous and intramonthly correlated). The intramonthly correlated solution shows significantly larger high-frequency variations than the continuous correlation solution and the OBP records. The continuous series (blue) has been shifted up by 10 cm, and the intramonthly series (red) has been shifted down 10 cm to aid the comparison.

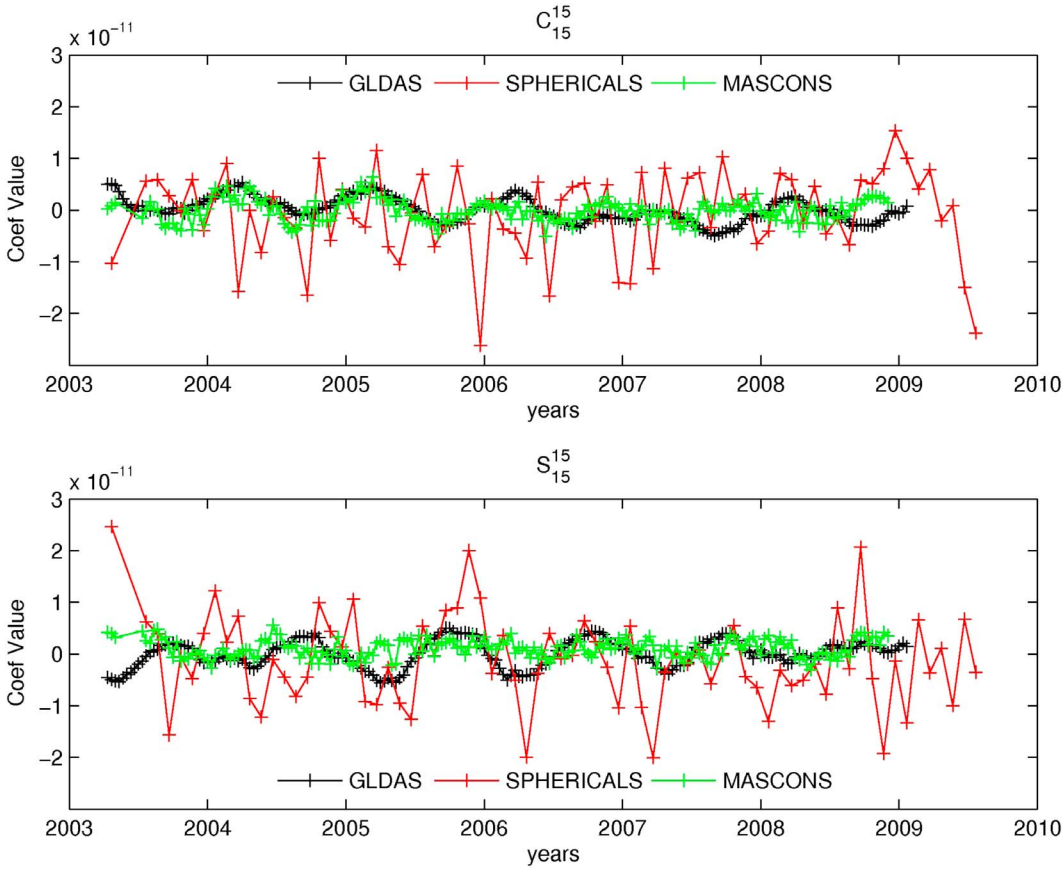

Figure 8. Time series of C_{15}^{15} and S_{15}^{15} Stokes coefficients from our preferred mascon solution at a 10 day sampling interval (green), from a series of Stokes coefficients estimated independently at monthly intervals (red), and the GLDAS series at a 10 day sampling interval (black).

hydrology forward model is a larger component of the mass signal than the residual signal recovered by GRACE. Over land this makes it almost impossible to present a determination of mass flux as observed purely by GRACE. Over oceans (as explained in section 4) our implementation of the hydrology model is at very low spatial resolution. The main advantage of a global hydrology forward model to oceans areas is the prevention of signal leakage from land areas and any spatial variation in the final determination of mass flux over oceans (the estimated mascons added to the hydrology model) arises solely from the mascons parameters. We avoid the disadvantages over land areas and preserve the advantages over the oceans by forming a hybrid model from two solutions. The ocean areas are extracted from a global solution in which GLDAS hydrology is used as a forward model (V06) and the land areas are extracted from a solution in which hydrology is not modeled (V05). Our preferred hybrid solution is mainly determined by GRACE over the oceans (is not dominated by the implementation of the hydrology model over ocean areas) and is completely determined by GRACE over land. It should be noted that the land V05 portion of the solution uses a value of $T = 10$ days while the ocean V06 portion uses a value of $T = 20$ days. These were chosen to accommodate the different signal-to-noise ratio characteristics of each portion.

[57] For example, the RMS annual amplitude over land for the V05 continuously time-correlated solution is 7.92 cm while the fit about the trend and annual signal is about 4.16 cm (see Table 1). In the same solution, the RMS annual amplitude over the oceans is 2.18 cm while the fit about the trend and annual signal is 3.0 cm. When the V05 solution is repeated with $T = 20$ days (instead of 10 days), the RMS annual amplitude decreases by only 2 mm (10%) while the fit about the signal drops by 1 cm (33%) and the signal becomes as large as the noise.

[58] The fact that our preferred global solution is really two regional solutions sewn together in no way prevents us from constructing the corresponding Stokes coefficients. In Figure 8 we plot the d/o 15 coefficients of several time series: (1) our preferred mascon solution, (2) a time series of GSFC monthly estimates of Stokes coefficients similar to those described in the work of *Luthcke et al.* [2006a], and (3) the GLDAS hydrology model. The d/o 15 resonance for GRACE is known to be a problem in time series in which standard Stokes coefficients are estimated in separate uncoupled solutions for each time period [*Swenson and Wahr*, 2006]. Figure 8 shows that our preferred solution is very well behaved at d/o 15.

[59] Finally, in Figure 9 we present the standard deviation of the mass flux from the series corresponding to our preferred solution. Figure 9 is plotted directly (without any post solution smoothing) from the Stokes coefficients (given to d/o 120) of our preferred solution. There is very little

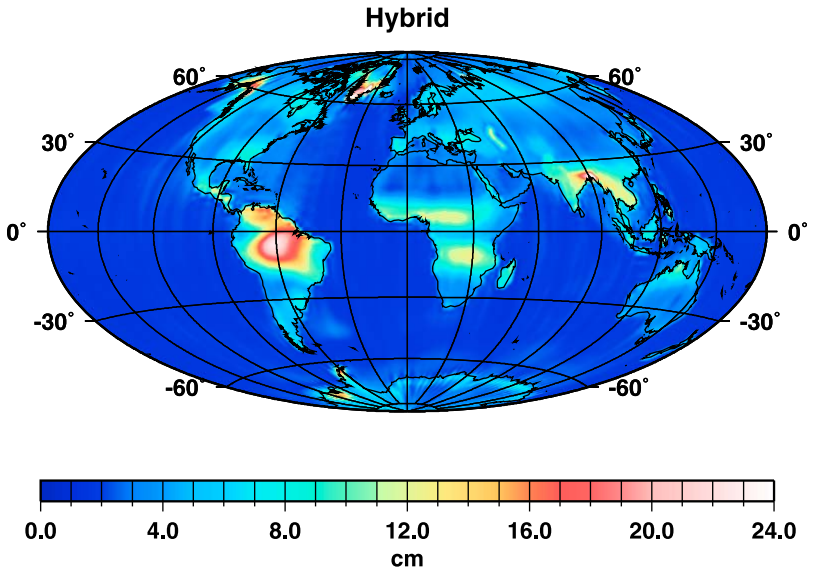

Figure 9. Standard deviation expressed in centimeters of equivalent water height for the preferred hybrid GRACE solution in which forward modeling of hydrology was used over the oceans where $T = 20$ days, but not over land where $T = 10$ days. A value of $D = 200$ km was used over all regions.

streaking and areas of known geophysical signal are clearly isolated.

7. Conclusions

[60] A mascon parameterization of time-variable gravity combined with reasonable physical constraints provides a powerful tool for analyzing mass flux processes seen by GRACE KBRR measurements. We have placed this approach in the context of other filtering techniques and have shown that it is as versatile as any of the other methods currently in use. Indeed, it can be interpreted as an ANS filter in which consistent pairs of Stokes coefficient states and full covariance matrices are combined with physically motivated and targeted constraints, which is straight forward due to the localized space/time nature of the mascons. We have interpreted the time constraints in terms of linear dynamical systems and have shown that these allow for a broad range of behavior with respect to correlation times. These arguments clearly translate into analogous properties in our spatial constraints as well. Exploitation of the Kronecker product structure of these constraints into spatial and temporal factors allows for a very efficient solution algorithm (in both storage and computation) to be realized based upon the PCG method.

[61] While the GRACE KBRR measurements can sense the center of a gravity source, the gravity signal can be spread over a wide area resulting in leakage. We have shown that the removal of dominant, known sources, particularly hydrology, greatly reduces this contamination. This forward modeling, as we call it, provides vast improvement over areas, for instance, north and south of the Amazon basin. In addition, removal of these periodic (seasonal) signals justifies the use of the monotonically nonincreasing autocorrelation functions we are implicitly assuming in our temporal constraint structure. Forward modeling also leads to KBRR residuals that more closely conform to zero-mean Gaussian distributions, which is an assumption of least squares.

[62] The process dynamics underlying the time-variable gravity signals are almost surely correlated through time and we can now build this continuous correlation into our estimators. We have shown that this generally results in solutions with reduced random variance, but not reduced power of systematic signals when compared to solutions incorporating only piecewise time correlation.

[63] This has culminated into a strategy for producing a preferred global solution, a hybrid, in which forward modeling of hydrology removes leakage in the ocean basins portion of the model and a relative decrease in T allows for higher autocorrelations at greater lags as would be expected when not removing the hydrological signals in the land portion of the model. The result is a model with minimal contamination over the oceans that is purely GRACE derived over land.

Appendix A: Dynamical Properties and Interpretation

[64] The dynamics of the filter are completely determined by the $\widetilde{\mathbf{Z}}$ matrix of equation (34) and may be interpreted as the response through time to an impulse $\mathbf{m}_0$ introduced at time $t_1 = 0$ in the presence of stochastic forcings $\overline{\mathbf{u}}$ by solving for $\mathbf{m}$ in the bottom portion of equation (32) such that

$$\mathbf{m} = -\overline{\mathbf{G}}^{-1}(\overline{\mathbf{u}} - \overline{\mathbf{a}}). \tag{A1}$$

Observe that since our $\overline{\mathbf{G}} = -\widetilde{\mathbf{G}} \otimes \mathbf{I}$, where $\widetilde{\mathbf{G}}$ is a $K \times K$ lower-triangular matrix, and $\mathbf{B1} = \mathbf{0}$, then by the multiplication of Kronecker products we have

$$\left(\widetilde{\mathbf{G}} \otimes \mathbf{I}\right)(\mathbf{1} \otimes \mathbf{m}_0) = \mathbf{e}_1 \otimes \mathbf{m}_0 = -\overline{\mathbf{a}}, \tag{A2}$$

where $\mathbf{e}_1$ is a unit vector whose first element is one and otherwise zero. This is an important general property of our filter since it means that the impulse $\mathbf{m}_0$ will persist through time and will not decay away; an infinite-memory filter. Contrast this with a Kalman filter in which $\widetilde{\mathbf{G}}$ is lower bidiagonal with $\widetilde{\mathrm{G}}_{kk} = 1$ for $k = 1, \ldots, K$ and $\widetilde{\mathrm{G}}_{k,k-1} = -\beta$ for $k = 2, \ldots, K$ with $0 < \beta < 1$. Clearly the row-sums for rows $k = 2, \ldots, K$ do not vanish and the result is a presence of $\mathbf{m}_0$ that decays away with time in the kth interval by the factor β^{k-1}; a limited memory filter. *Kurtenbach et al.* [2009] also use the Kalman filter, but impose the infinite-memory property shared by our filter by choosing $\beta = 1$.

[65] The inversion of Kronecker products leads to $-\overline{\mathbf{G}}^{-1} = \widetilde{\mathbf{G}}^{-1} \otimes \mathbf{I}$, and so $\widetilde{\mathbf{G}}^{-1}$ actually determines the interplay between $\mathbf{m}_0$ and $\overline{\mathbf{u}}$. A description of its precise behavior as a function of T and t_{ij} over nonuniform intervals is beyond the scope of this paper. However, we can provide this for uniform intervals, which is the situation for most cases. Let Δt be the constant duration of the uniform intervals and let $\xi = \exp(1)$ and $\rho = \exp(-\Delta t/T)$. It then follows from equations (27) and (34) that

$$\widetilde{\mathrm{Z}}_{ij} = \begin{cases} \xi\left(\dfrac{\rho}{1-\rho}\right)(2 - \rho^{i-1} - \rho^{K-i}) & , \quad i = j \\ -\xi\rho^{|i-j|} & , \quad i \neq j \end{cases}, \tag{A3}$$

$$\widetilde{\mathrm{G}}_{ij} = \begin{cases} 1 & , \quad i = j \\ 0 & , \quad i < j \\ -\left(\dfrac{1-\rho}{1-\rho^{i-1}}\right)\rho^{i-j-1} & , \quad i > j \end{cases}, \tag{A4}$$

$$\widetilde{\mathrm{G}}^{-1}_{ij} = \begin{cases} 1 & , \quad i = j \\ 0 & , \quad i < j \\ \dfrac{1-\rho}{1-\rho^{j}} & , \quad i > j \end{cases}. \tag{A5}$$

[66] For a fixed Δt we can look at two extreme cases: (1) for very long T such that $\lim_{T\to\infty} \rho = 1$; denoted the "$T_\infty$" case, and (2) for very short T such that $\lim_{T\to 0} \rho = 0$; denoted the "T_0" case. The results are

$$\widetilde{\mathrm{G}}^{-1}_{ij} = \begin{cases} \left.\begin{array}{ll} 1, & i = j \\ 0, & i < j \\ \dfrac{1}{j}, & i > j \end{array}\right\} & T_\infty \\ \left.\begin{array}{ll} 0 & , \quad i < j \\ 1 & , \quad i \geq j \end{array}\right\} & T_0 \end{cases}. \tag{A6}$$

It turns out that $\widetilde{\mathbf{G}}^{-1}$ for the "T_0" case is identical to that of the Kalman filter used by *Kurtenbach et al.* [2009] and represents a classic "random walk" starting from $\mathbf{m}_0$ at $t_1 = 0$ with the kth step being $\mathbf{u}_k$.

[67] Because $\mathbf{u}_k$ is random we cannot know in advance the value of $\mathbf{m}_k$ for $k = 1, \ldots, K$, but we can determine its probabilistic position and uncertainty of this position by using $\overline{\mathbf{U}}$. As can be seen from equation (35), with the exception of the force $\mathbf{u}_0$ on the initial impulse, our filter readily provides this information. If we assume an independent identical spatial distribution, then it has the form $\mathbf{u}_k \sim \mathcal{N}(\mathbf{0}, \sigma_k^2\,\mathbf{I})$ for $k = 1, \ldots, K-1$, where $\sigma^2_{k-1} = \lambda^{-1}\,\mathrm{B}^{-2}_{kk}$ and λ is a general scaling factor (actually the damping factor in equation (35)). Our filter does not provide $\mathbf{u}_0$, but we can assume a similar form of $\mathbf{u}_0 \sim \mathcal{N}(\mathbf{0}, \sigma_0^2\,\mathbf{I})$. It then follows immediately from the linearity of equation (A1) that

$$\mathrm{E}[\mathbf{m}_k] = \mathbf{m}_0, \tag{A7}$$

$$\mathrm{C}\left[\mathbf{m}_k, \mathbf{m}_{k'}\right] = \left[\sum_{j=1}^{k} \sigma^2_{j-1}\widetilde{\mathrm{G}}^{-1}_{kj}\widetilde{\mathrm{G}}^{-1}_{k'j}\right]\mathbf{I} = c_{kk'}\,\mathbf{I}, \tag{A8}$$

where $\mathrm{E}[\cdot]$ and $\mathrm{C}[\cdot, \cdot]$ are the expectation and covariance operators, respectively. Because $\widetilde{\mathrm{G}}^{-1}_{k,1} = 1$, the σ_0^2 value serves as a constant offset to the $c_{kk'}$ values provided by the filter. If we let $\overline{\sigma}_k^2 = c_{kk}$, then this leads to the following general variance/covariance expressions for $k = 1, \ldots, K-1$ and $j = k+2, \ldots, K$, seeded with $\overline{\sigma}_1^2 = \sigma_0^2$:

$$\sigma_k^2 = \frac{\lambda^{-1}}{\xi\rho}\left(\frac{1-\rho}{1-\rho^k}\right)\left[1 + \rho\left(\frac{1-\rho^{K-k-1}}{1-\rho^{k+1}}\right)\right]^{-1}, \tag{A9}$$

$$\overline{\sigma}^2_{k+1} = \overline{\sigma}^2_k + \left\{\sigma_k^2 + \left[\left(\frac{1-\rho}{1-\rho^k}\right)^2 - 1\right]\sigma^2_{k-1}\right\}, \tag{A10}$$

$$c_{k+1,j} = \overline{\sigma}^2_{k+1} + \left(\frac{1-\rho}{1-\rho^{k+1}} - 1\right)\sigma_k^2. \tag{A11}$$

The recursive relationships are a result of the sub-diagonal portion of each column of $\widetilde{\mathbf{G}}^{-1}$ being constant.

[68] For the end-member cases the expressions in equations (A9)–(A11) reduce to

$$\left.\begin{array}{rcl} \sigma_k^2 & = & \dfrac{\lambda^{-1}}{\xi K}\left(\dfrac{k+1}{k}\right) \\ \overline{\sigma}^2_{k+1} & = & \sigma_0^2 + \sigma_1^2 \\ c_{k+1,j} & = & \sigma_0^2 + \dfrac{1}{2}\sigma_1^2 \end{array}\right\} \quad T_\infty$$

$$\left.\begin{array}{rcl} \sigma_k^2 & = & \dfrac{\lambda^{-1}}{\xi\rho} \\ \overline{\sigma}^2_{k+1} & = & \sigma_0^2 + k\sigma_1^2 \\ c_{k+1,j} & = & \sigma_0^2 + k\sigma_1^2 \end{array}\right\} \quad T_0 \tag{A12}$$

Note that to keep the variances finite in the "T_0" case, we must choose λ proportional to ρ^{-1}. The results are inter-

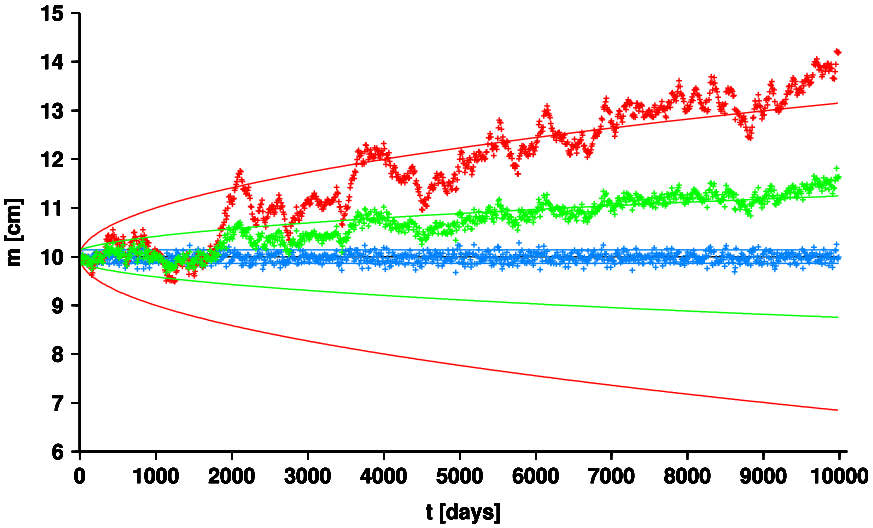

Figure A1. Example of time series of a single mascon governed by a linear dynamical system reflecting the covariance structure of the temporal constraints used in GSFC mascon solutions. A perfectly known ($\sigma_0^2 = 0$ cm^2) initial impulse of $m_0 = 10$ cm is introduced at $t_1 = 0$ days and evolves through time in the presence of a stochastic force u_{k-1} at step k for $K = 1000$ steps. Three cases are shown: (1) an extreme case in which T is much longer than the interval duration Δt (blue), (2) an extreme case in which T is much shorter than the interval duration (red), and (3) an intermediate case in which $T = 20$ days and $\Delta t = 10$ days (green). The plus symbols show m_k, while the smooth curves define the $1 - \sigma$ probability zone, where m_k is likely to be located. The black horizontal line indicates m_0. The variances in case (2) are set to $\sigma_k^2 = 0.01$ cm^2, for $k = 1, \ldots, K - 1$, and the variances for the other two cases are scaled such that all mean variances over the time span of interest are equivalent.

esting in that the level-σ curves of the probability distribution function of position range from the classic $\sqrt{k}$ functionality with step k for the "T_0" or "random walk" case (if we choose $\sigma_0^2 = \sigma_1^2$) to a constant function with step k for the "T_∞" case. We shall see that for infinitely long series ($K \to \infty$), the "T_∞" case becomes a "white noise" process about $\mathbf{m}_0$. Clearly, this range is asymptotically obtainable in our scheme by proper choices of T.

[69] These properties can be illustrated by showing examples of time series of a single mascon governed by a linear dynamical system reflecting the covariance structure of the temporal constraints used in GSFC mascon solutions. Three cases are explored, the two end-member cases and an intermediate case similar to one considered in this paper in which $T = 20$ days and $\Delta t = 10$ days. We assume a perfectly known ($\sigma_0^2 = 0$ cm^2) impulse of $m_0 = 10$ cm is introduced at $t_1 = 0$ days and draw from a single set of independently distributed $u_k \sim \mathcal{N}(0, 1)$ for $k = 1, \ldots, K - 1$, which are then scaled to the appropriate σ_k^2 level for each case. We choose λ such that $\sigma_k^2 = 0.01$ cm^2 for the "T_0" case and then scale the other cases such that all mean variances over the time-span of interest are equivalent. We run the systems for $K = 1000$ steps. Figure A1 shows the three time series where the "T_∞" and "T_0" cases are indicated in blue and red, respectively, and the intermediate case is in green. The "+" symbols show m_k while the smooth curves define the 1-σ probability zone where m_k is likely to be located. The black horizontal line indicates m_0. The continuum from the "random walk" to the "white noise" process with increasing T can be clearly seen. However, what might not be so obvious is the autocorrelation of the time series, especially as a function of duration of the series, which is one of the most familiar properties used in designing filters.

Appendix B: Autocorrelation

[70] The autocovariance γ_L of a discrete time series of length K for a single mascon m at lag L is given by [*Davis*, 1973]

$$\gamma_L = \frac{1}{K - L - 1} \sum_{j=1}^{K-L} \left(m_j - \mu_L^b\right)\left(m_{j+L} - \mu_L^e\right), \tag{B1}$$

where m_j and m_{j+L} are the mascon values at discrete times t_j and t_{j+L}, respectively, and μ_L^b and μ_L^e are the mean values computed from the series subsets $\{m_1, \ldots, m_{K-L}\}$ and $\{m_{L+1}, \ldots, m_K\}$, respectively. The expected value of γ_L over an ensemble of such time series for this particular mascon can be directly related to the covariance matrix in equation (A8) for a single mascon, denoted $\mathbf{C}_m$, through simple propagation as

$$\mathrm{E}[\gamma_L] = \frac{1}{K - L - 1} \mathrm{Tr}\left[\mathbf{J}_L \mathbf{K}_L^b \mathbf{C}_m \mathbf{K}_L^e\right], \tag{B2}$$

where Tr[·] is the trace operator, $\mathbf{J}_L$ is a matrix whose Lth subdiagonals are all ones and otherwise zero, and

$$\mathbf{K}_L^b = \begin{pmatrix} \mathbf{K}_L & \mathbf{0} \\ \mathbf{0} & \mathbf{0} \end{pmatrix}, \quad \mathbf{K}_L^e = \begin{pmatrix} \mathbf{0} & \mathbf{0} \\ \mathbf{0} & \mathbf{K}_L \end{pmatrix}. \tag{B3}$$

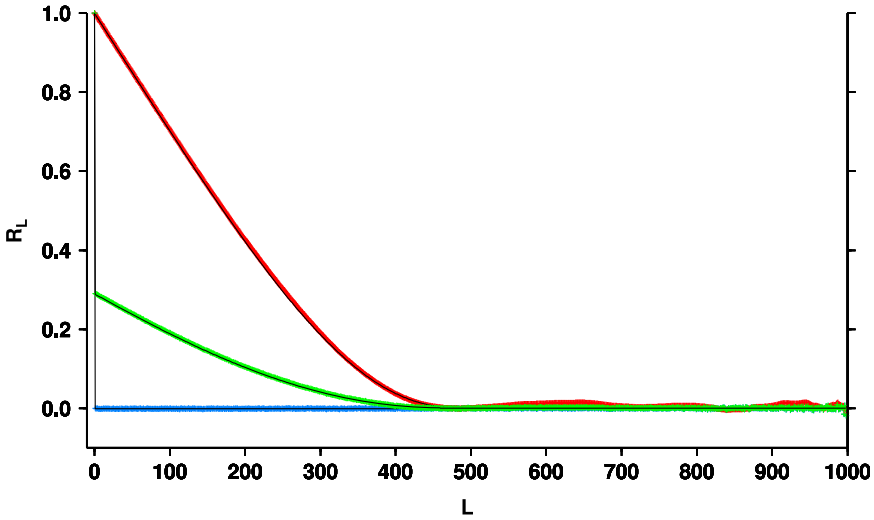

Figure B1. The autocorrelation functions R_L as a function of lag L corresponding to the three cases shown in Figure A1, except here the intermediate case uses $T = 200$ days. The colored plus symbols are computed with $\mathrm{E}[\gamma_L]$, $\mathrm{E}[\gamma_L^b]$, and $\mathrm{E}[\gamma_L^e]$ from an ensemble average of equations (B1), (B4), and (B5), respectively, using 3000 sample time series, while the black curves are computed with $\mathrm{E}[\gamma_L]$, $\mathrm{E}[\gamma_L^b]$, and $\mathrm{E}[\gamma_L^e]$ directly from equations (B2), (B6), and (B7), respectively.

Here $\mathbf{K}_L = \mathbf{I} - \frac{1}{K-L}\mathbf{1}\mathbf{1}^{\mathrm{T}}$ is a $(K-L)\times(K-L)$ projection matrix which removes the mean from a length-$(K-L)$ vector. The associated variances for the two series subsets γ_L^b and γ_L^e are given by

$$\gamma_L^b = \frac{1}{K-L-1}\sum_{j=1}^{K-L}\left(m_j - \mu_L^b\right)^2, \tag{B4}$$

$$\gamma_L^e = \frac{1}{K-L-1}\sum_{j=L+1}^{K}\left(m_j - \mu_L^e\right)^2, \tag{B5}$$

and their expected values over an ensemble of such time series are

$$\mathrm{E}\left[\gamma_L^b\right] = \frac{1}{K-L-1}\mathrm{Tr}\left[\mathbf{K}_L^b\mathbf{C}_m\mathbf{K}_L^b\right], \tag{B6}$$

$$\mathrm{E}\left[\gamma_L^e\right] = \frac{1}{K-L-1}\mathrm{Tr}\left[\mathbf{K}_L^e\mathbf{C}_m\mathbf{K}_L^e\right]. \tag{B7}$$

The autocorrelation R_L over the ensemble at lag L is then given by

$$R_L = \mathrm{E}[\gamma_L]/\sqrt{\mathrm{E}[\gamma_L^b]\mathrm{E}[\gamma_L^e]}. \tag{B8}$$

[71] Approximations to equations (B1), (B4), and (B5) can be made when $K \gg L$ such that μ_L^b and μ_L^e can be replaced by the mean value over the entire series and γ_L^b and γ_L^e can be replaced by the variance over the entire series γ_0 [see *Wilks*, 2006]. In this situation, equation (B8) can be evaluated, after extensive algebra, for the end-member cases such that

$$R_L = \begin{cases} \left.\begin{array}{ll} 1 & , \quad L = 0 \\ -\frac{1}{K}\frac{1-LK^{-1}}{1-(L+1)K^{-1}} & , \quad L > 0 \end{array}\right\} & T_\infty \\ \\ \dfrac{1-5LK^{-1}+(6L^2-1)K^{-2}+L(1-2L^2)K^{-3}}{1-LK^{-1}-(L+1)K^{-2}} & T_0 \end{cases}. \tag{B9}$$

For an infinitely long series, i.e., $K \to \infty$, and a finite lag L' these approach $R_{L'} = \delta_{L'}$ for the "T_∞" and $R_{L'} = 1$ for the "T_0" cases, where $\delta_{L'}$ is the Kronecker delta.

[72] We can now make a connection with the classic definition of "correlation time" T_c in the context of infinite first-order Markov chains in which $R_L = \exp(-L\Delta t/T_c)$ [*Gelb*, 1974], and so $R_L = e^{-1}$ at time $L\Delta t = T_c$. The "random walk" and "white noise" cases occur when $T_c \to \infty$ and $T_c \to 0$, respectively, but this is in contrast to the $T \to 0$ and $T \to \infty$ respective conditions needed for the same. Since *Rowlands et al.* [2010] define the a priori variance of $m_{j+L} - m_j$ as $\tilde{\sigma}_L^2 = \lambda^{-1}\xi^{-1}\rho^{-L}$, then we see that $T = \tilde{\sigma}_L^2/(\tilde{\sigma}_L^2)_t$, where $(\cdot)_t$ is the derivative operator with respect to $t = L\Delta t$, and so it may be more appropriate to call T the "characteristic time" of $\tilde{\sigma}_L^2$ rather than a "correlation time." Because the structure of the spatial constraints is similar to that of the temporal constraints used in GSFC mascon solutions, a similar argument applies to the terminology used in describing D.

[73] Figure B1 shows the autocorrelation functions that correspond to the three cases in Figure A1, except here the

intermediate case uses $T = 200$ days in order to accentuate the variation of R_L with T. In fact, the R_L of the intermediate case in Figure A1 would fall very close to the "T_0" curve. Because R_L is a monotonically nonincreasing function of L, we can determine T_c as the time at which $R_L = e^{-1}$, although some correlation time definitions use $R_L = 0$. For the case of $\Delta t = 10$ days, $T = 20$ days, and $K = 197$, it takes approximately $T_c = 400$ days for R_L to decrease to a value of e^{-1} and $T_c = 970$ days for R_L to vanish.

[74] Ultimately, only the upper-right $(K - L) \times (K - L)$ portion of $\mathbf{C}_m$ is operated on in equation (B2). The structure of $\mathbf{C}_m$ revealed in equation (A11) shows that post-multiplication by $\mathbf{K}_L^e$ makes $\mathrm{E}[\gamma_L]$, and therefore R_L, vanish when $L \geq \left\lceil \frac{K+1}{2} \right\rceil$ for all values of T, where the $\lfloor \cdot \rfloor$ operator indicates "the largest integer not greater than" the argument. This is indeed evident in Figure B1.

[75] **Acknowledgments.** Support for this work was provided by NASA through the GRACE Science team. We gratefully acknowledge the quality of GRACE Level 1B products produced by our colleagues at the Jet Propulsion Laboratory. We also thank the NCCS at GSFC for computational resources. Jean-Paul Boy is currently visiting NASA Goddard Space Flight Center, with a Marie Curie International Outgoing Fellowship (PIOF-GA-2008-221753). We would like to thank three anonymous reviewers and the Associate Editor for their useful insights and suggestions.

References

Brooks, D. H., G. F. Ahmad, R. S. MacLeod, and G. M. Maratos (1999), Inverse electrocardiography by simultaneous imposition of multiple constraints, *IEEE Trans. Biol. Eng.*, *46*, 3–18, doi:10.1109/10.736746.

Carrere, L., and F. Lyard (2003), Modeling the barotropic response of the global ocean to atmospheric wind and pressure forcing—Comparisons with observations, *Geophys. Res. Lett.*, *30*(6), 1275, doi:10.1029/2002GL016473.

Chambers, D. P. (2006), Observing seasonal steric sea level variations with GRACE and satellite altimetry, *J. Geophys. Res.*, *111*, C03010, doi:10.1029/2005JC002914.

Chao, B. F., W. P. O'Conner, A. T. C. Chang, D. K. Hall, and J. L. Foster (1987), Snow load effects on the Earth's rotation and gravitational field 1979–1985, *J. Geophys. Res.*, *92*(B9), 9415–9422, doi:10.1029/JB092iB09p09415.

Chen, J. L., M. Rodell, C. R. Wilson, and J. S. Famiglietti (2005), Low degree spherical harmonic influences on Gravity Recovery and Climate Experiment (GRACE) water storage estimates, *Geophys. Res. Lett.*, *32*, L14405, doi:10.1029/2005GL022964.

Davis, J. C. (1973), *Statistics and Data Analysis in Geology*, John Wiley, New York.

Demmel, J. W. (1997), *Applied Numerical Linear Algebra*, SIAM, Philadelphia, Pa.

Drevillon, M., L. Parent, N. Ferry, E. Greiner, and B. Barnier (2009), Global ocean reanalysis simulations at Mercator Océan GLORYS1: The Argo years 2002–2008, *Eos Trans. AGU*, *90*(52), Fall Meet. Suppl., Abstract OS22A–04.

Flechtner, F. (2007), Gravity recovery and climate experiment; AOD1B product description document for Product Releases 01 to 04, *GRACE Rev 3.1*, 327–750.

Gelb, A. (1974), *Applied Optimal Estimation*, MIT Press, Cambridge, Mass.

Golub, G. H., and C. F. Van Loan (1989), *Matrix Computations*, 2nd ed., Johns Hopkins Univ. Press, Baltimore, Md.

Higham, N. (1990), Analysis of the Cholesky decomposition of a semidefinite matrix, in *Reliable Numerical Computation*, edited by M. G. Cox and S. J. Hammarling, pp. 161–185, Oxford Univ. Press, Oxford, U. K.

Klees, R., E. A. Revtova, B. C. Gunter, P. Ditmar, E. Oudman, H. C. Winsemius, and H. H. G. Savenije (2008), The design of an optimal filter for monthly GRACE gravity models, *Geophys. J. Int.*, *175*, 417–432, doi:10.1111/j.1365-246X.2008.03922.x.

Kurtenbach, E., T. Mayer-Gürr, and A. Eicker (2009), Deriving daily snapshots of the Earth's gravity field from GRACE L1B data using Kalman filtering, *Geophys. Res. Lett.*, *36*, L17102, doi:10.1029/2009GL039564.

Kusche, J. (2007), Approximate decorrelation and nonisotropic smoothing of time-variable GRACE-type gravity field models, *J. Geod.*, *81*, 733–749, doi:10.1007/s00190-007-0143-3.

Laub, A. J. (2005), *Matrix Analysis for Scientists and Engineers*, SIAM, Philadelphia, Pa.

Lev-Ari, H. (2005), Efficient solution of linear matrix equations with application to multistatic antenna array processing, *Commun. Inf. Syst.*, *5*, 123–130.

Luthcke, S. B., D. D. Rowlands, F. G. Lemoine, S. M. Klosko, D. S. Chinn, and J. J. McCarthy (2006a), Monthly spherical harmonic gravity field solutions determined from GRACE inter-satellite range-rate data alone, *Geophys. Res. Lett.*, *33*, L02402, doi:10.1029/2005GL024846.

Luthcke, S. B., H. J. Zwally, W. Abdalati, D. D. Rowlands, R. D. Ray, R. S. Nerem, F. G. Lemoine, J. J. McCarthy, and D. S. Chinn (2006b), Recent Greenland ice mass loss by drainage system from satellite gravity observations, *Science*, *314*, 1286, doi:10.1126/science.1130776.

Luthcke, S. B., A. A. Arendt, D. D. Rowlands, J. J. McCarthy, and C. F. Larsen (2008), Recent glacier mass changes in the Gulf of Alaska region from GRACE mascon solutions, *J. Glaciol.*, *54*, 767–777, doi:10.3189/002214308787779933.

Moritz, H. (1980), *Advanced Physical Geodesy*, Abacus, Kent, U. K.

Ray, R. D. (1999), A global ocean tide model from TOPEX/POSEIDON altimetry: GOT99.2, *Tech. Rep. 1999–209478*, NASA Goddard Space Flight Cent., Greenbelt, Md.

Ray, R. D., and R. M. Ponte (2003), Barometric tides from ECMWF operational analyses, *Ann. Geophys.*, *21*, 1897–1910, doi:10.5194/angeo-21-1897-2003.

Rodell, M., et al. (2004), The Global Land Data Assimilation System, *Bull. Am. Meteorol. Soc.*, *85*(3), 381–394, doi:10.1175/BAMS-85-3-381.

Rowlands, D. D., R. D. Ray, D. S. Chinn, and F. G. Lemoine (2002), Short-arc analysis of intersatellite tracking data in a gravity mapping mission, *J. Geod.*, *76*, 307–316, doi:10.1007/s00190-002-0255-8.

Rowlands, D. D., S. B. Luthcke, S. M. Klosko, F. G. Lemoine, D. S. Chinn, J. J. McCarthy, C. M. Cox, and O. B. Anderson (2005), Resolving mass flux at high spatial and temporal resolution using GRACE intersatellite measurements, *Geophys. Res. Lett.*, *32*, L04310, doi:10.1029/2004GL021908.

Rowlands, D. D., S. B. Luthcke, J. J. McCarthy, S. M. Klosko, D. S. Chinn, F. G. Lemoine, J.-P. Boy, and T. J. Sabaka (2010), Global mass flux solutions from GRACE: A comparison of parameter estimation strategies: Mass concentrations versus Stokes coefficients, *J. Geophys. Res.*, *115*, B01403, doi:10.1029/2009JB006546.

Swenson, S., and J. Wahr (2002), Methods for inferring regional surface-mass anomalies from Gravity Recovery and Climate Experiment (GRACE) measurements of time-variable gravity, *J. Geophys. Res.*, *107*(B9), 2193, doi:10.1029/2001JB000576.

Swenson, S., and J. Wahr (2006), Postprocessing removal of correlated errors in GRACE data, *Geophys. Res. Lett.*, *33*, L08402, doi:10.1029/2005GL025285.

Tapley, B. D., S. V. Bettadpur, M. Watkins, and C. Reighber (2004), The Gravity Recovery and Climate Experiment mission overview and early results, *Geophys. Res. Lett.*, *31*, L09607, doi:10.1029/2004GL019920.

Toutenburg, H. (1982), *Prior Information in Linear Models*, John Wiley, New York.

Velicogna, I., and J. Wahr (2006), Acceleration of Greenland ice mass loss in spring 2004, *Nature*, *443*, 329–331, doi:10.1038/nature05168.

Wilks, D. S. (2006), *Statistical Methods in the Atmospheric Sciences*, 2nd ed., Academic, New York.

Wouters, B., D. Chambers, and E. J. O. Schrama (2008), GRACE observes small-scale mass loss in Greenland, *Geophys. Res. Lett.*, *35*, L20501, doi:10.1029/2008GL034816.

Wu, X., R. G. Blom, E. R. Ivins, F. A. Oyafuso, and M. Zhong (2009), Improved inverse and probabilistic methods for geophysical applications of GRACE gravity data, *Geophys. J. Int.*, *177*, 865–877, doi:10.1111/j.1365-246X.2009.04141.x.

Zhang, Y., A. Ghodrati, and D. H. Brooks (2005), An analytical comparison of three spatiotemporal regularization methods for dynamic linear inverse problems in a common statistical framework, *Inverse Problems*, *21*, 357–382, doi:10.1088/0266-5611/21/1/022.

J.-P. Boy, S. B. Luthcke, D. D. Rowlands, and T. J. Sabaka, Planetary Geodynamics Laboratory, Code 698, NASA Goddard Space Flight Center, Greenbelt, MD 20771, USA. (Terence.J.Sabaka@nasa.gov)